nature neuroscience

Article

https://doi.org/10.1038/s41593-025-01972-9

Choroid plexus apocrine secretion shapes CSF proteome during mouse brain development

Received: 21 February 2024

Accepted: 3 April 2025

Published online: 28 May 2025

Check for updates

Ya'el Courtney[1,2], Joshua P. Head[1], Neil Dani[1,3], Olga V. Chechneva[4], Frederick B. Shipley[1,5], Yong Zhang[6], Michael J. Holtzman[6], Cameron Sadegh[4], Towia A. Libermann[7] & Maria K. Lehtinen[1,2,5]

The choroid plexus (ChP) regulates cerebrospinal fluid (CSF) composition, providing essential molecular cues for brain development; yet, embryonic ChP secretory mechanisms remain poorly defined. Here we identify apocrine secretion by embryonic ChP epithelial cells as a key regulator of the CSF proteome and neurodevelopment in male and female mice. We demonstrate that the activation of serotonergic 5-HT$_{2C}$ receptors (by WAY-161503) triggers sustained Ca^{2+} signaling, driving high-volume apocrine secretion in mouse and human ChP. This secretion alters the CSF proteome, stimulating neural progenitors lining the brain's ventricles and shifting their developmental trajectory. Inducing ChP secretion in utero in mice disrupts neural progenitor dynamics, cerebral cortical architecture and offspring behavior. Additionally, illness or lysergic acid diethylamide exposure during pregnancy provokes coordinated ChP secretion in the mouse embryo. Our findings reveal a fundamental secretory pathway in the ChP that shapes brain development, highlighting how its disruption can have lasting consequences for brain health.

Cerebrospinal fluid (CSF)-borne factors play essential roles in regulating the central nervous system throughout life[1,2]. The epithelial cells of the choroid plexus (ChP), located in each brain ventricle, are a principal source of CSF[3] and introduce many of these secreted factors[1,4]. Disrupting the balance of CSF-borne signals during embryonic development can impair neural progenitor proliferation and cause brain abnormalities that persist into adulthood[5]. Despite the developmental importance of these factors, how embryonic ChP cells regulate exocytosis remains unclear. Therefore, it has been difficult to identify real-life threats to healthy brain development that may act by disrupting the ChP–CSF axis. Gaining insight into what regulates ChP secretion will improve our understanding of brain development and highlight potential developmental hazards.

Ca^{2+} signaling is a broadly conserved mechanism by which cells regulate secretion. A growing body of research implicates serotonergic receptor 5-HT$_{2C}$ (a G_q/G_{11}-coupled G-protein-coupled receptor encoded by *Htr2c*) as a mediator of ChP Ca^{2+} activity[6] and protein release. Activating 5-HT$_{2C}$ in primary ChP epithelial cell cultures increases Ca^{2+} activity and leads to secretion of transferrin[7] and insulin[8], although the involved exocytosis mechanisms have not been examined. We recently developed an in vivo ChP imaging approach for adult mice, demonstrating that ChP 5-HT$_{2C}$ can be activated by selective synthetic

[1]Department of Pathology, Boston Children's Hospital and Harvard Medical School, Boston, MA, USA. [2]Graduate Program in Neuroscience, Harvard Medical School, Boston, MA, USA. [3]Department of Cell and Developmental Biology, Vanderbilt University, Nashville, TN, USA. [4]Department of Neurosurgery, University of California, Davis, Sacramento, CA, USA. [5]Graduate Program in Biophysics, Harvard University, Cambridge, MA, USA. [6]Pulmonary and Critical Care Medicine, Department of Medicine, Washington University School of Medicine, St. Louis, MO, USA. [7]Proteomics, Bioinformatics and Systems Biology Center, Beth Israel Deaconess Medical Center and Harvard Medical School, Boston, MA, USA. e-mail: maria.lehtinen@childrens.harvard.edu

agonist WAY-161503 (ref. 9), leading to a sustained rise in intracellular Ca^{2+}, activity-dependent gene expression and observations of both vesicular fusion and high-volume secretion events[10].

Because the embryonic ChP also expresses high levels of *Htr2c*[11], we hypothesized that activating the receptor might lead to Ca^{2+}-dependent secretion of bioactive signals into the CSF, potentially targeting CSF-contacting apical progenitor cells and impacting cerebral cortical development. We tested this hypothesis by developing an ex vivo imaging approach for embryonic ChP. We found that embryonic exposure to a 5-HT_{2C} agonist activates ChP epithelial cells and alters the CSF proteome, introducing numerous factors that likely act combinatorially to tune progenitor fate. We demonstrate that overactivating ChP secretion during brain development is accompanied by abnormal cerebral cortical formation and adult behavior. We also report a type of calpain-dependent ChP protein release analogous to apocrine secretion reported in other glandular epithelia[12] and demonstrate the vulnerability of the embryonic ChP–CSF system to disruption by maternal exposure to serotonergic and nonserotonergic insults.

Results

5-HT_{2C} agonist activates embryonic ChP

We tracked real-time Ca^{2+} activity in embryonic day 16.5 (E16.5) ex vivo mouse embryos and developed a two-photon imaging strategy in embryonic mice where ChP epithelial cells expressed the Ca^{2+} reporter GCaMP6f (using *Ai95D* mice[13] crossed with *FoxJ1-cre* mice that target this cell population[14]). Baseline Ca^{2+} activity in embryonic fourth ventricle (4V) ChP epithelial cells was captured in vivo using two-photon microscopy (Fig. 1a). Delivery of the 5-HT_{2C} agonist WAY-161503 into the 4V activated Ca^{2+} signaling in ChP epithelial cells (Fig. 1b,c and Supplementary Video 1), demonstrating that embryonic ChP responds to 5-HT_{2C} activation following direct exposure to WAY-161503.

Maternal exposure to WAY-161503 via subcutaneous injection propagated to the embryo and activated the developing ChP, inducing activity-dependent gene *Fos* expression (Extended Data Fig. 1a). In additional control studies using *Htr2c*-knockout mice (*Htr2c*^{tm1Jke}/J), we confirmed that ChP *Htr2c* expression was necessary for activation by WAY-161503 (Extended Data Fig. 1b–d). Embryonic ChP response to maternal–fetal drug transfer was impacted by maternal anesthesia, which has implications for maternal–fetal drug transfer studies and para-uterine imaging preparations[15]. Isoflurane inhibited E16.5 ChP *Fos* induction in response to maternal WAY-161503 injection (Extended Data Fig. 1a). Ketamine/xylazine maintained most of the *Fos* response but is not ideal for extended anesthesia. Intraperitoneal (i.p.) urethane followed by ketamine allowed stable anesthesia for several hours and mostly preserved the ChP response (Extended Data Fig. 1e). These observations demonstrate that the embryonic ChP is sensitive to maternal transmission of signals and motivated us to investigate whether WAY-161503-stimulated Ca^{2+} activity led to exocytosis.

Embryonic ChP activation triggers apocrine secretion

In mice, cerebral cortical neurogenesis primarily occurs from E10.5 to E16.5 (ref. 16; Fig. 1d). The lateral ventricle (LV) ChP, nearest to the ventricular zone (VZ) where these progenitors reside, is specified and begins to differentiate around E9.5 (ref. 17). In the developing mouse brain, *Htr2c* was highly and selectively expressed in ChP epithelial cells from E12 to E16.5 (Extended Data Fig. 2)[18–20]. Maternal subcutaneous administration of WAY-161503 triggered ChP activation as early as E12.5, as evaluated by Fos protein expression (Fig. 1e and Extended Data Fig. 3a; control = 2.06 ± 0.19 versus WAY-161503 = 8.18 ± 0.13, $P = 0.0004$, two-tailed t-test). Maternal WAY-161503 exposure retained the ability to activate the ChP throughout neurogenesis (for example, E14.5 and E16.5), as evaluated by *Fos* gene transcription (Fig. 1f). This activation was accompanied by the formation of large secretory structures in most embryonic ChP epithelial cells (71.4% at E14.5 and 77.0% at E16.5; Fig. 1g,h). These structures, called aposomes, are evidence of apocrine secretion, an exocytosis process in which glandular epithelial cells release a large, protein-rich cytoplasmic bolus into a fluid-filled lumen[12]. Aposomes were present on 20.4% of E14.5 and 22.5% of E16.5 ChP epithelial cells without stimulation (Fig. 1g,h), suggesting a baseline frequency of secretion that was accelerated in a widespread, synchronized manner following 5-HT_{2C} activation.

We identified embryonic ChP aposomes by scanning electron microscopy (SEM), transmission electron microscopy, hematoxylin and eosin (H&E) staining and immunostaining (Extended Data Fig. 3b–g). Each ChP epithelial cell produced a single aposome, which arose from a depression in the center of the apical membrane immediately adjacent to the ciliary bundle (Fig. 1i, Extended Data Fig. 3c–e and Supplementary Video 2). When a cell was not forming an aposome, this apical depression was identifiable from its absence of staining for ChP epithelial cell surface proteins, including ezrin (Extended Data Fig. 3f). The aposome was supported by a network of microtubules (Extended Data Fig. 3g and Supplementary Video 3) and protruded an average of 5 µm from the cell surface (Extended Data Fig. 3h). The percentage of ChP cells capable of apocrine secretion appeared consistent in embryonic and adult ChP (72.1%; Extended Data Fig. 3i,j).

Protein-retention expansion microscopy[21] revealed that ChP aposomes contained essential cargo, including transthyretin (TTR; Fig. 1j and Supplementary Video 4), a carrier protein that transports thyroid hormones critical for normal embryonic brain development and the maintenance of proper neuronal function[22]. Consistent with these data and human ChP expression of *HTR2C*[23], human gestational week 21 (GW21) ChP treated ex vivo with WAY-161503 for 1 h formed TTR-filled aposomes (Fig. 1j). A bicinchoninic acid (BCA) assay of conditioned medium from human GW21 LV ChP showed increased protein concentration following incubation with WAY-161503 (control = 0.28 mg ml^{-1} versus 0.5 µM WAY-161503 = 0.36 mg ml^{-1}). BCA assays (Fig. 1k) and silver staining (Extended Data Fig. 3k) of mouse CSF collected at baseline or following 5-HT_{2C} stimulation

Fig. 1 | Maternal–fetal activation of ChP 5-HT_{2C} evokes apocrine secretion of proteins into the CSF. a, Placenta-attached ex vivo imaging setup. **b**, Overview image of exposed E16.5 4V ChP and time points showing tissue Ca^{2+} response to WAY-161503. **c**, Heat map of E16.5 ChP cellular Ca^{2+} responses to direct WAY-161503 (WAY) exposure. **d**, Timeline of readouts of apocrine secretion. **e**, Representative confocal images of E12.5 mouse brain 30 min after maternal saline (control) or WAY-161503 delivery; scale bars 100 µm. **f**, RT–qPCR analysis of ChP *Fos* expression at E14.5 (left; $N = 11$ embryos, three litters) and E16.5 (right; $N = 10$ embryos, three litters). *F*, fluorescence. **g**, Quantification of the data in **h**; $N = 20$ embryos, four litters per condition. **h**, SEM of E14.5 (top) and E16.5 (bottom) LV ChP; scale bars, 20 µm. **i**, Representative confocal images of E16.5 LV ChP 30 min after maternal WAY-161503 delivery; scale bars, 20 µm; Ac-Tubulin, acetylated tubulin. **j**, Top: protein-retention expansion microscopy of E16.5 LV ChP 30 min after maternal WAY-161503 delivery. Bottom: fetal GW21 LV control ChP (left) or after a 30-min incubation with WAY-161503 (right). White arrows indicate TTR-containing aposomes. Scale bars, 10 µm. **k**, E12.5, E14.5 and E16.5 CSF protein concentration (conc.) 30 min after maternal saline (E12.5 $N = 4$, E14.5 $N = 7$, E16.5 $N = 8$) or WAY-161503 (E12.5 $N = 3$, E14.5 $N = 6$, E16.5 $n = 7$) delivery. Each point represents pooled CSF from one litter. **l**, Western blot for TTR and SOD3 in E16.5 mouse CSF. A cropped Ponceau stain of each membrane is displayed as a loading control. **m**, Western blot for TTR from human ChP-conditioned artificial CSF (aCSF) following exposure to WAY-161503 or vehicle control. A cropped Coomassie blue stain is displayed as a loading control. Full blots and stains are shown in Supplementary Fig. 2. All data are presented as mean ± s.e.m. *P* values were calculated by two-way analysis of variance (ANOVA) with a Sidak correction for **f**, **g** and **k**. Images in **b** represent experiments repeated three times with similar results, in **i** represent experiments repeated ten times with similar results and in **l** represent experiments repeated five times with similar results. The experiment in **m** was only performed once. Panel **d** created with BioRender.com.

https://doi.org/10.1038/s41593-025-01972-9

revealed that apocrine secretion was associated with the increased presence of many proteins. Targeted approaches confirmed increased availability of the antioxidant superoxide dismutase 3 (SOD3) and TTR in embryonic mouse CSF (Fig. 1l) and release of TTR by human ChP exposed to WAY-161503 ex vivo (Fig. 1m). In agreement with descriptions of apocrine secretion in other epithelia[24], organelles, including mitochondria, were observed in apocrine structures (Extended Data Fig. 3l).

Programmed cell death (apoptosis) is a well-characterized event that results in the apical extrusion of unhealthy cells from epithelial sheets[25]. To confirm that the structures we identified as aposomes were not apoptotic bodies, we performed cleaved caspase-3 staining. We did not observe any evidence of apoptosis accompanying apocrine secretion (Extended Data Fig. 4). Following secretion, the number of ChP aposomes returned to baseline after 24 h, when a full apocrine response could again be evoked by 5-HT$_{2C}$ activation (Extended Data Fig. 3m).

Embryonic ChP apocrine secretion shifts the CSF proteome

To catalog the contents of embryonic apocrine secretion, we conducted an untargeted analysis of proteins in E16.5 CSF at baseline versus 30 min following 5-HT$_{2C}$-induced apocrine secretion using the SomaScan v4.1 aptamer-based proteomics platform[26]. CSF samples were controlled for the absence of blood contamination (Extended Data Fig. 5). Analysis revealed 101 proteins increased in E16.5 CSF

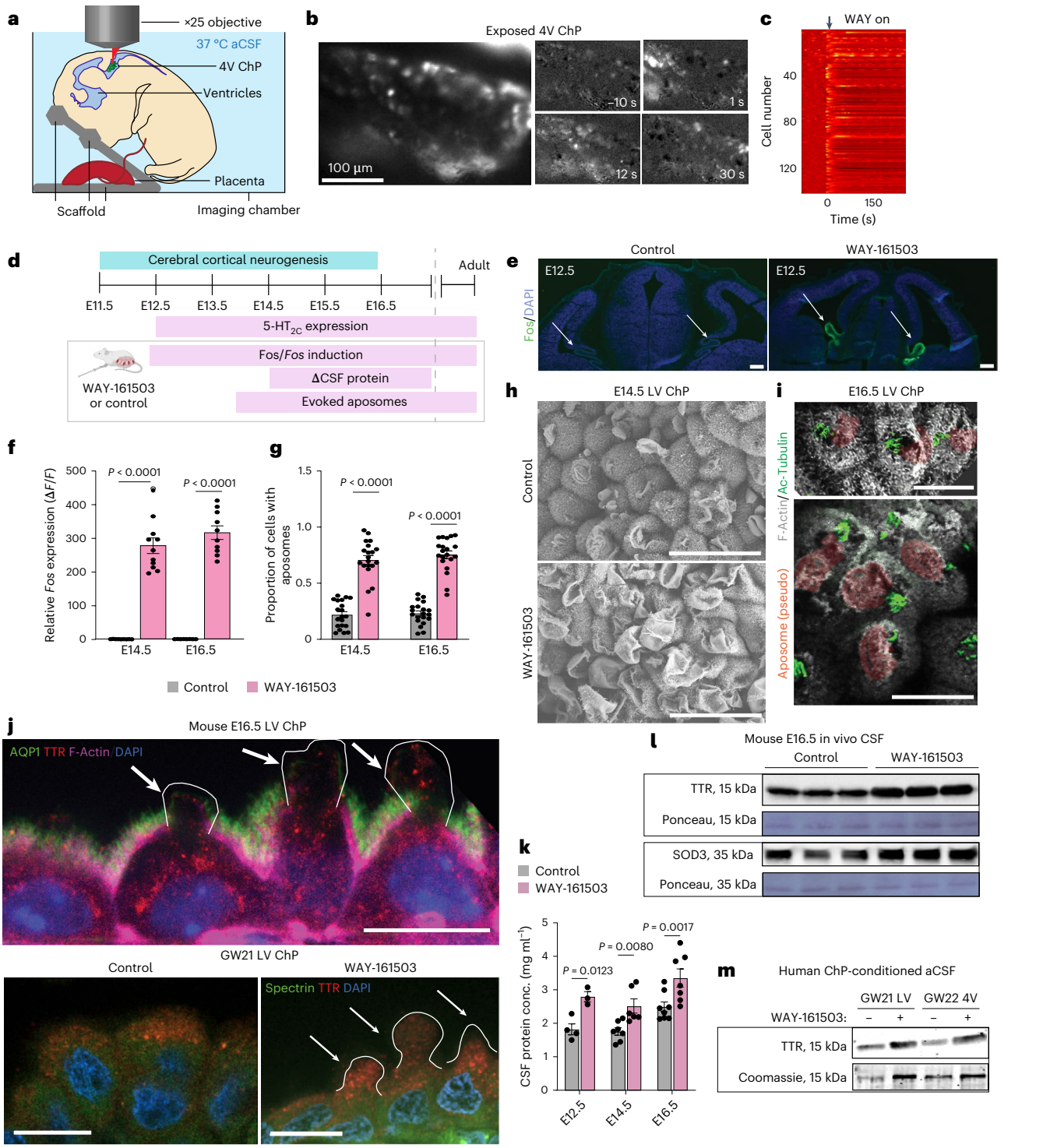

https://doi.org/10.1038/s41593-025-01972-9

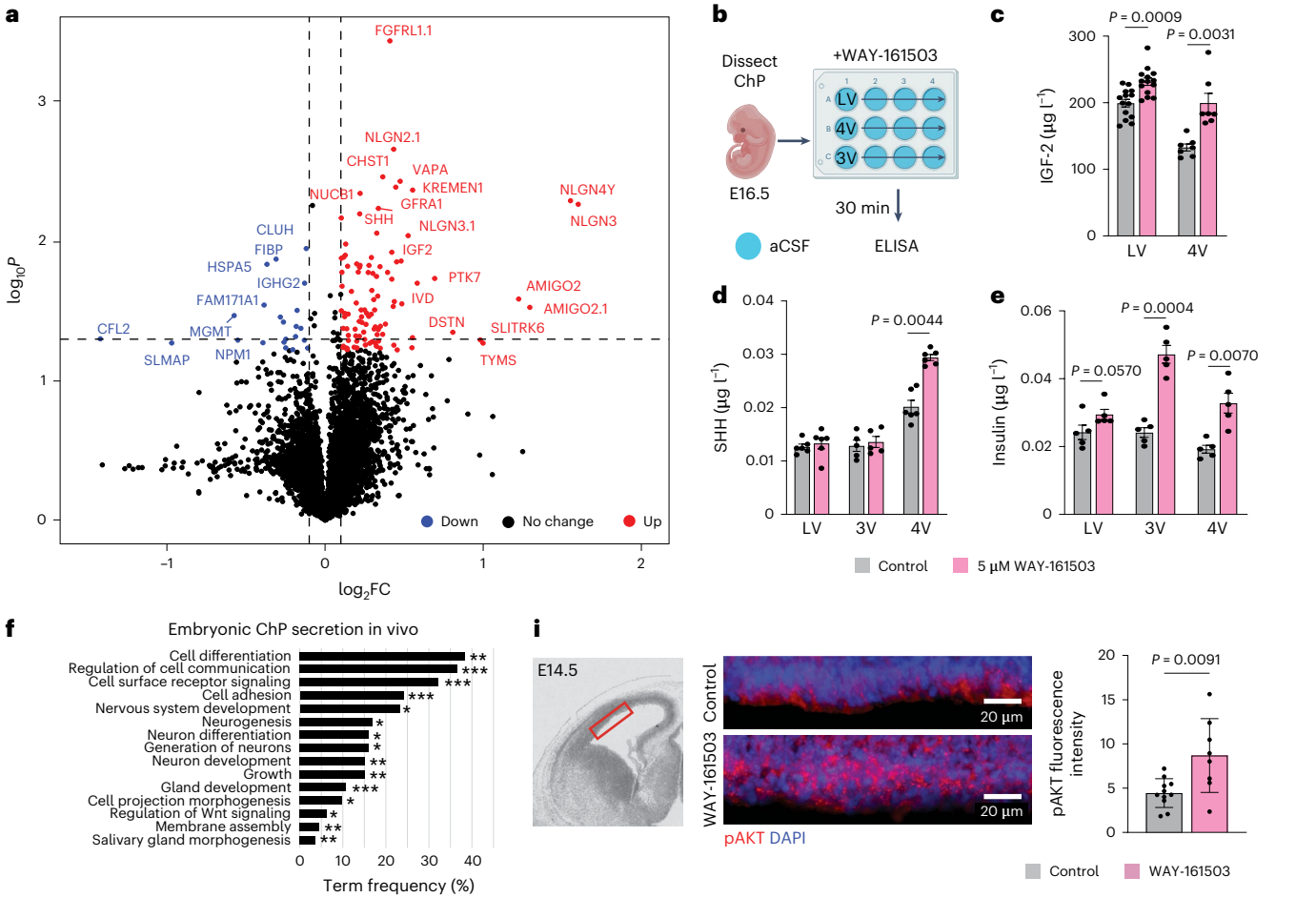

Fig. 2 | Apocrine secretion alters the embryonic CSF proteome. a, Volcano plot showing differences in protein abundance between E16.5 CSF at baseline and following apocrine secretion. Proteins with *P* values less than 0.05 appear above the horizontal dashed line. The vertical dashed lines indicate the threshold of ±1.1 fold change (FC); *N* = 3 pooled litters per condition. **b**, Experimental schematic for data presented in **c** and **d**. **c**, Enzyme-linked immunosorbent assay (ELISA) of explant-conditioned aCSF for IGF-2. Each point represents aCSF conditioned by five E16.5 ChP explants; LV *N* = 14, 3V *N* = 7, 4V *N* = 7. **d**, ELISA of explant-conditioned aCSF for SHH. Each point represents aCSF conditioned by five E16.5 ChP explants; LV *N* = 6, 3V *N*= 5, 4V *N* = 6. **e**, ELISA of explant-conditioned aCSF for insulin. Each point represents aCSF conditioned by five E16.5 ChP explants; LV *N* = 5, 3V *N* = 5, 4V *N* = 5. **f**, Biological pathways identified by GSEA for proteins released in vivo by ChP 5-HT_{2C}-evoked secretion. A one-sided, right-tailed Fisher's exact test was used to assess over-representation of pathways ($P < 0.05$), as our analysis focused specifically on identifying enrichment in the observed direction of change; ns, not significant ($P > 0.05$); *$P \leq 0.05$; **$P \leq 0.01$; ***$P \leq 0.001$; ****$P \leq 0.0001$. **g**,**h**, IPA of ChP in vivo secreted proteins demonstrated activation of proliferation- and development-related pathways (**g**) and activation of neuronal survival, neurite outgrowth and synapse development pathways and inhibition of neuronal apoptosis (**h**). **i**, Left: Nissl annotation from the Allen Developing Mouse Brain Reference Atlas[69] (developingmouse.brain-map.org). Confocal images of phosphorylated AKT (pAKT) in E14.5 neural progenitor cells (center) and quantification of pAKT fluorescence intensity (right) are also shown (control *N* = 11, three litters; WAY-161503 *N* = 8, three litters); scale bars, 20 µm. All data are presented as mean ± s.e.m. *P* values were calculated by one-way ANOVA with a Tukey correction for **c**–**e**, a one-sided Fisher's exact test for **f** and a two-tailed *t*-test for **i**. Panel **b** created with BioRender.com.

following maternal WAY-161503 exposure (false discovery rate-adjusted $P < 0.05$; Fig. 2a, Supplementary Table 1 and Supplementary Data 1). Among those increased were two proteins with neurodevelopmental relevance: insulin-like growth factor 2 (IGF-2) and sonic hedgehog (SHH; Extended Data Fig. 6a). CSF IGF-2 stimulates progenitor cell proliferation and is required for healthy cortical development[5], and CSF SHH contributes to proper brain size and hindbrain development[27]. Using a ChP explant-conditioned medium approach (Fig. 2b), we validated the release of IGF-2, SHH and insulin following 5-HT_{2C} activation. ChP tissues are patterned with ventricle-specific transcriptomes and secretomes[4,11]. We observed similar IGF-2 release into the conditioned medium by mouse LV and 4V ChP (Fig. 2c). *IGF2* is also expressed by human ChP[4,23]. Using human ChP explants, we observed IGF-2 release into conditioned medium in two of three specimens after incubation with WAY-161503 (Extended Data Fig. 6b; GW21 LV ChP: control = 6.17 pg ml^{-1} versus 0.5 µM WAY-161503 = 6.79 pg ml^{-1}; GW21 LV ChP: control = 6.64 pg ml^{-1} versus 5 µM WAY-161503 = 6.61 pg ml^{-1}; GW22 4V ChP: control = 5.57 pg ml^{-1} versus 5 µM WAY-161503 = 5.91 pg ml^{-1}). For transcripts known to have regionalized expression across mouse ChP[5,15], we confirmed robust SHH release by 4V ChP (Fig. 2d) and the highest insulin release by third ventricle (3V) ChP[8] (Fig. 2e). In addition to IGF-2 and SHH, we observed increases in several other proteins in the CSF following 5-HT_{2C}-induced apocrine secretion (Supplementary Table 2), including angiopoietin-1 (+11%), neuregulin-1 (NRG1; +10%), macrophage migration inhibitory factor (MIF; +15%), ephrin-A5 (+40%) and PDGFA (+10%).

One limitation of aptamer-based proteomics is the occasional occurrence of proteins incorrectly identified as decreased in abundance due to post-translational modifications that prevent aptamer binding. For example, in our postsecretion CSF SomaScan analysis, the results suggested decreased cofilin-2, but by contrast, targeted approaches revealed that it was increased but phosphorylated at serine 3, thereby preventing its accurate detection (Extended Data Fig. 6c).

Toward understanding the biological implications of CSF changes arising from 5-HT_{2C} activation, we used gene set enrichment analysis (GSEA) and Ingenuity Pathway Analysis (IPA; Qiagen) to reveal interactions between secreted CSF proteins and their potential downstream targets. GSEA revealed an over-representation of biological pathways with implications for neural development, including neurogenesis, neuron differentiation and regulation of Wnt signaling (Fig. 2f and Extended Data Fig. 2). IPA revealed networks of protein interactions supporting neuron quantity, proliferation and development (Fig. 2g) and activating neural survival pathways while inhibiting neuronal cell death and apoptosis pathways (Fig. 2h). Together, these analyses support the model that embryonic ChP secretion provides a CSF niche favorable to cell viability and introduces signals likely to affect the fate of VZ neural progenitors. Indeed, we found that E14.5 VZ progenitors had increased phosphorylated AKT 30 min following ChP secretion (Fig. 2i), suggesting that VZ progenitors respond to altered CSF contents. The observed array of secreted proteins with neurodevelopmental relevance and the concurrent activation of neural progenitors prompted us to examine what would happen to cerebral cortical development if ChP secretion were overstimulated during neurogenesis.

Overstimulating ChP secretion disrupts cortical development

We overstimulated ChP secretion by administering WAY-161503 to pregnant dams, either acutely at E12.5 or chronically with repeated, once daily injections from E12.5 to E16.5. At postnatal day 8 (P8), we evaluated the offspring's gross brain morphology, distribution of excitatory neurons marked by CTIP2, SATB2 and TBR1 and glial cell populations, and at P30, we examined inhibitory interneurons marked by parvalbumin (PV) or somatostatin (SST) expression (Fig. 3a). After chronically overstimulating ChP secretion, we did not observe differences in gross brain morphology or cerebral cortical cell density at P8 (Fig. 3b and Extended Data Fig. 7a–c). However, we observed increased $SATB2^+$ neurons and fewer $TBR1^+$ neurons in the primary somatosensory

Fig. 3 | Embryonic overstimulation of ChP secretion is accompanied by abnormal cerebral cortical development. a, Schematic depicting experiment and readouts. **b**, S1 cortical cell density is unchanged in E12.5–E16.5 (*N* = 10 mice, four litters) or E12.5 (*N* = 8 mice, three litters) WAY-161503 exposure experimental groups versus vehicle control (*N* = 15 mice, four litters). **c**, Quantification of $CTIP2^+$, $TBR1^+$ and $SATB2^+$ neuronal populations in P8 S1 in vehicle control (*N* = 15 mice, four litters), E12.5 WAY-161503 (*N* = 8 mice, three litters) and E12.5–E16.5 (*N* = 10 mice, four litters) experimental groups. **d**, Top: confocal images of SATB2 (green) in the S1. Bottom: $SATB2^+$ neuron proportion by bin (vehicle control *N* = 13 mice, four litters; E12.5–E16.5 WAY-161503 *N* = 10 mice, three litters; E12.5 WAY-161503 *N*= 5 mice, three litters). **e**, Top: confocal images of TBR1 (green) in the S1. Bottom: $TBR1^+$ neuron proportion by bin (vehicle control *N* = 7 mice, three litters; E12.5–E16.5 WAY-161503 *N* = 10 mice, three litters; E12.5 WAY-161503 *N* = 5 mice, three litters). **f**, Top: confocal images of CTIP2 (green) in the S1. Bottom: $CTIP2^+$ neuron proportion by bin (vehicle control *N*= 7 mice, three litters; E12.5–E16.5 WAY-161503 *N* = 10 mice, three litters; E12.5 WAY-161503 *N* = 8 mice, three litters). **g**, Top: representative confocal images of PV and SST interneurons in the S1. Bottom: percentage of nuclei in the S1 or primary motor cortex (M1) labeled by PV or SST (vehicle control *N* = 9 mice, three litters; E12.5–E16.5 WAY-161503 *N* = 7 mice, three litters; E12.5 WAY-161503 *N* = 6 mice, three litters); scale bars, 100 µm. **h**, Confocal images (left) and quantification (right) of the percentage of $GFAP^+$ coverage in the S1, hippocampus (HC) and corpus callosum (CC; vehicle control *N* = 9 mice, three litters; E12.5–E16.5 WAY-161503 *N* = 13 mice, four litters); scale bars, 50 µm. **i**, Confocal images (left) and quantification (right) of $IBA1^+$ microglia in the S1, hippocampus and corpus callosum (vehicle control *N* = 9 mice, three litters; E12.5–E16.5 WAY-161503 *N* = 13 mice, four litters); scale bars, 50 µm. All data are presented as mean ± s.e.m. Regions of interest depicted in **d**–**f** are 1,000 µm tall by 400 µm wide. *P* values were calculated by two-way ANOVA with a Sidak correction for **b**–**g** and by one-way ANOVA with a Tukey correction for **h** and **i**. Data points in **d**–**g** represent the mean of three technical replicate stainings performed on three serial sections per biological replicate mouse. Data points in **h** and **i** represent the mean of three fields of view per biological replicate mouse. Panel **a** created with BioRender.com.

https://doi.org/10.1038/s41593-025-01972-9

cortex (S1; Fig. 3c). Across all cerebral cortical layers, SATB2$^+$ neurons increased by 20.6%, TBR1$^+$ neurons decreased by 53.3%, and CTIP2$^+$ neurons remained unaffected. We divided the cerebral cortex into six equally sized bins to ascertain the relationship between these cell population changes and appropriate cortical layering. This analysis revealed that population changes were driven by alterations in the deeper cortical layers reflected in bins 4, 5 and 6. SATB2$^+$ populations increased by 48.1% in bin 4, 52.6% in bin 5 and 78.0% in bin 6 (Fig. 3d).

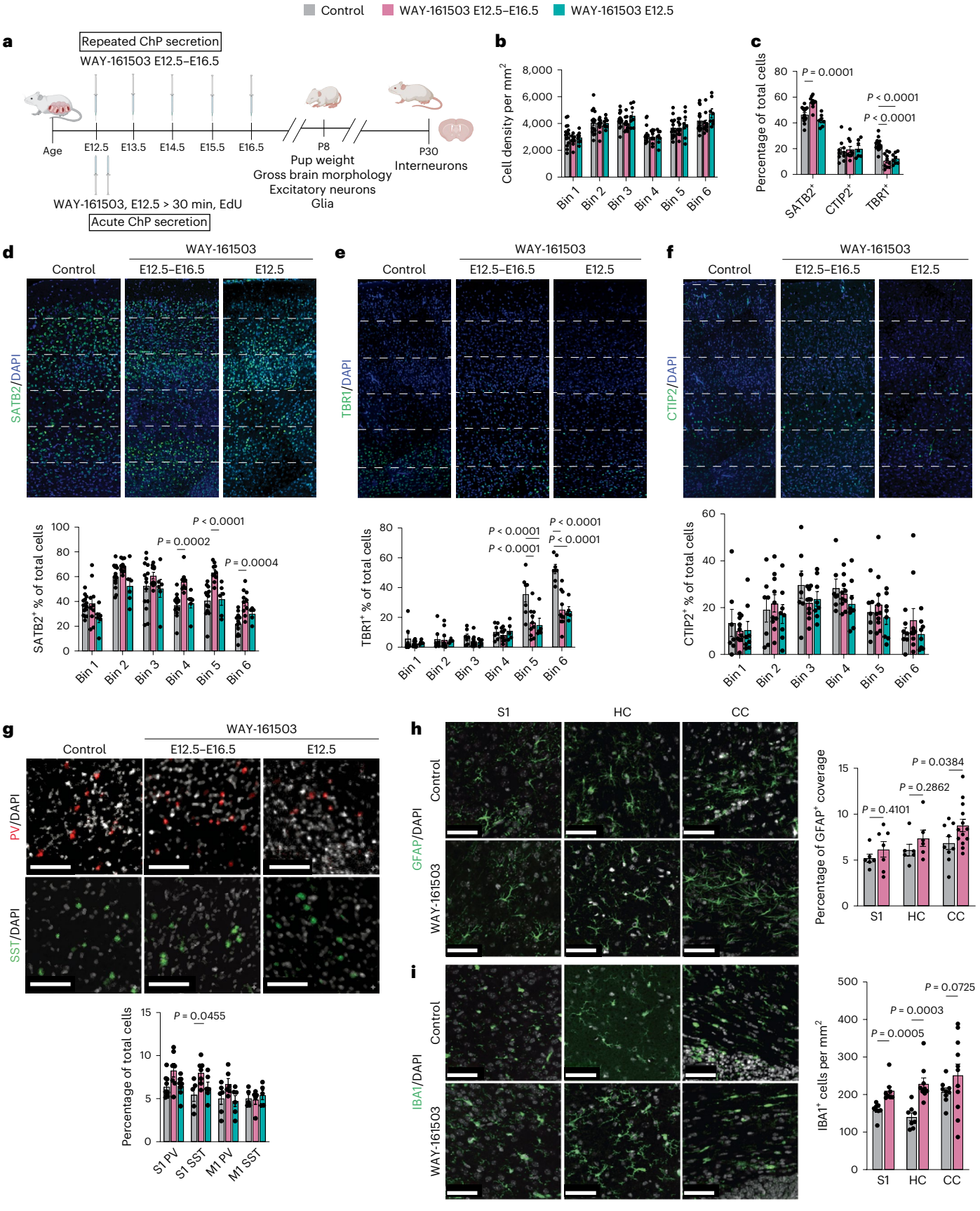

TBR1$^+$ populations decreased by 53.5% in bin 5 and 51.8% in bin 6 (Fig. 3e). CTIP2$^+$ populations were not altered (Fig. 3f).

These data suggest that repeatedly overstimulating apocrine secretion in pregnant mice is associated with altered offspring cortical excitatory neuron populations, decreasing deep-layer TBR1$^+$ corticothalamic neurons but increasing deep-layer SATB2$^+$ callosal projection neurons. When ChP secretion was evoked acutely at E12.5, we observed a similar reduction in deep-layer TBR1$^+$ neurons (Fig. 3e) not accompanied by increased deep-layer SATB2$^+$ neurons (Fig. 3d). These findings indicate that the cumulative effects of repeated ChP overstimulation are necessary to drive the observed increase in SATB2$^+$ neurons. Repeated overstimulation was also accompanied by a 46.9% increase in S1 SST$^+$ interneurons (Fig. 3g), a 28.1% increase in GFAP$^+$ astrocyte coverage in the corpus callosum (Fig. 3h) and increased IBA1$^+$ microglia in the S1 (+31.3%) and hippocampus (+63.1%; Fig. 3i). Repeated overstimulation did not affect the number of white matter oligodendrocytes or oligodendrocyte precursors (Extended Data Fig. 7d–f).

We paired acute WAY-161503 at E12.5 with EdU labeling to trace proliferative activity and cell cycle dynamics in the cerebral cortex and ganglionic eminences (Fig. 4a,b). At 2 h following treatment, phospho-histone H3$^+$ (PHH3$^+$) cells increased by 20.4% in the cortical VZ (Fig. 4c–e), indicating heightened mitotic activity. No changes were observed in the lateral ganglionic eminence (LGE) or medial ganglionic eminence (MGE). Concurrently, EdU$^+$ cell density increased by 35.6% in the LGE (Fig. 4g), reflecting a proliferative response in this subcortical region, while no changes were observed in the cortex or MGE (Fig. 4f,h). By 18 h, PHH3$^+$ cells were no longer elevated in any region examined (Fig. 4i–k). Meanwhile, EdU$^+$ cell density decreased by 12.1% in the cortical plate/intermediate zone (CP/IZ; Fig. 4l), returned to baseline in the LGE (Fig. 4m) and remained unchanged in the MGE (Fig. 4n).

By P8, acute ChP overstimulation at E12.5 was associated with 44.9% fewer cortical EdU$^+$ cells overall, with strongest effects on deeper cortical layers (Fig. 4o). The differentiation of TBR1$^+$ neurons decreased by 48.2% after treatment (EdU$^+$TBR1$^+$ cells), and this decreased differentiation persisted after the period of EdU incorporation (−43.9% EdU$^-$ TBR1$^+$ cells; Fig. 4p). These data demonstrate that early perturbations in ChP activity are accompanied by disrupted progenitor dynamics and impaired generation of deep-layer cortical neurons that likely contribute to long-term cerebral cortical abnormalities.

Three behavioral assays were administered at P90 for assessing neurodevelopmental disorder-associated phenotypes: three-chamber social approach, marble burying and adult male–female ultrasonic vocalizations (USVs). Abnormal behavior arose in the three-chamber social approach task, where adult mice that had been exposed in utero to repeated apocrine stimulation (hereafter, 'repeated apocrine mice') displayed lower sociability than control mice (Fig. 5a). Distance traveled (Fig. 5b) was unchanged, suggesting that decreased time spent with the novel mouse was not attributable to motor deficits. Repeated apocrine mice buried fewer marbles in the marble burying task (Fig. 5c), a metric for assessing rodent repetitive behaviors. Marble burying was impacted by sex as a biological variable, with male mice burying fewer marbles and no change in female mice (Fig. 5d). Differences attributable to sex were not significant in other histological or behavioral analyses and were not due to differences in ChP *Htr2c* expression (Fig. 5e). In the USV task, repeated apocrine mice were more vocal, emitting more total courtship vocalizations (Fig. 5f), but did not initiate more physical interactions with the test mouse (Fig. 5g). When USVs were analyzed by subcategories based on frequency and pattern, the observed increase appeared nonspecific across most vocalizations (Fig. 5h).

Maternal LSD exposure triggers embryonic ChP apocrine secretion

Given that embryonic overactivation of ChP secretion could lead to life-long brain and behavioral changes, we examined a broader range of maternal stimuli for their potential to disrupt the ChP–CSF system. We used immunostaining and quantitative PCR with reverse transcription (RT–qPCR) to detect *Fos* expression and aposomes in the embryonic ChP 30 min following maternal exposure to a stimulus, identifying several conditions that triggered *Fos* induction and widespread aposomes in the E16.5 LV ChP.

We tested lysergic acid diethylamide (LSD) because psychedelic compounds, including LSD, act strongly at 5-HT$_{2C}$[28] and have been observed to bind at the adult ChP[29]. Maternal exposure to LSD (0.2 mg per kg (body weight)) resulted in transmission of the drug to the developing embryonic brain. Thirty minutes after subcutaneous administration of LSD to pregnant dams, we observed that LSD induced E16.5 ChP *Fos* expression and apocrine secretion (Fig. 6a). *Fos* expression increased by 70-fold compared to control, which, although smaller than the 380-fold increase observed with WAY-161503 (Fig. 6b), was still associated with sufficient activation to cause apocrine secretion. We observed aposomes in 68.3% of E16.5 ChP epithelial cells after LSD exposure, a 3.1-fold increase from baseline and similar to the 77.8% of cells with aposomes after WAY-161503 treatment (Fig. 6b). Given this evidence of maternal–fetal psychedelic transmission and ChP apocrine secretion, follow-up studies are warranted to explore the risks maternal psychedelic exposure may pose to healthy development.

Although 5-HT$_{2C}$ activation caused ChP apocrine secretion, it was not necessary for this process, as *Htr2c*-knockout mice[30] still displayed the same proportion of cells with aposomes at baseline (Extended Data Fig. 8a,b). Because 5-HT$_{2C}$ is a Gα_q-protein-coupled receptor that induces a rapid rise in intracellular Ca^{2+}, we considered whether apocrine secretion may be evoked by other processes that increase intracellular Ca^{2+}. We queried our ChP cell atlas[11] for epithelial expression of receptors associated with Ca^{2+} regulation in cells. Among highly expressed candidates was *Trpm3*, a heat-activated transient receptor potential cation channel subfamily M member 3 (TRPM3), which gates Na^+ and Ca^{2+}. When a TRPM3 agonist, CIM0216 (ref. 31), was administered subcutaneously to pregnant mice at E16.5, embryonic ChP aposomes increased more than threefold, and Fos protein expression was evident in 73.6% of epithelial nuclei, comparable to WAY-161503 (Fig. 6c,d).

Fig. 4 | Effects of ChP overstimulation on cortical and ganglionic eminence progenitor proliferation and differentiation. a, Schematic of experimental design. **b**, Diagram illustrating the analyzed regions of interest: cortex, LGE and MGE. **c**–**e**, Quantification and representative images of PHH3$^+$DAPI$^+$ mitotic nuclei per 10,000 µm^2 in the cortex (**c**; control $N = 13$; WAY-161503 $N = 13$), LGE (**d**; control $N = 10$; WAY-161503 $N = 14$) and MGE (**e**; control $N = 10$; WAY-161503 $N = 13$) at 2 h post-EdU. **f**, Quantification and representative images of EdU$^+$ nuclei in cortical CP/IZ and VZ regions at 2 h post-EdU (control $N = 13$; WAY-161503 $N = 15$). **g**,**h**, Quantification and representative images of EdU$^+$ nuclei per 10,000 µm^2 in the LGE (**g**; control $N = 9$; WAY-161503 $N = 12$) and MGE (**h**; control $N = 9$; WAY-161503 $N = 12$) at 2 h post-EdU. **i**–**k**, Quantification and representative images of PHH3$^+$DAPI$^+$ mitotic nuclei per 10,000 µm^2 in the cortex (**i**; control $N = 10$, WAY-161503 $N = 11$), LGE (**j**; control $N = 9$, WAY-161503 $N = 12$) and MGE (**k**; control $N = 10$, WAY-161503 $N = 9$) at 18 h post-EdU. **l**, Quantification and representative images of EdU$^+$ nuclei in cortical CP/IZ and VZ regions at 18 h post-EdU (control $N = 10$, WAY-161503 $N = 12$). **m**,**n**, Quantification and representative images of EdU$^+$ nuclei per 10,000 µm^2 in the LGE (**m**; control $N = 10$, WAY-161503 $N = 11$) and MGE (**n**; control $N = 10$, WAY-161503 $N = 10$) at 18 h post-EdU. **o**, Quantification and representative images of overall EdU$^+$ cell density at P8 in the cortex (control $N = 9$, WAY-161503 $N = 8$). **p**, Bar graphs depicting the percentage of TBR1$^+$EdU$^+$ cells (center) and TBR1$^+$EdU$^-$ cells (right) and representative images (left) of the S1 at P8 (control $N = 8$, WAY-161503 $N = 7$). All data are presented as mean ± s.e.m. *P* values were calculated by two-sided *t*-tests for **c**–**e**, **g**–**k**, **m** and **n**, two-way ANOVA with a Sidak correction for **f** and **l** and one-way ANOVA with a Tukey correction for **p**; scale bars, 50 µm (**c**–**e** and **i**–**k**), 100 µm (**f**–**h** and **l**–**n**) and 200 µm (**o** and **p**). All *N* indicate the number of mice collected from three separate litters. Panel **a** created with BioRender.com.

https://doi.org/10.1038/s41593-025-01972-9

Diverse stimuli converge on the ChP apocrine pathway

Subsequent ChP explant culture experiments showed that apocrine secretion in ChP cells is initiated by several key intracellular pathways activated through 5-HT$_{2C}$ and TRPM3 signaling, which were identified using pathway blockers (Fig. 6e). We used D609 to inhibit phospholipase C[32] (PLC), FIPI to inhibit phospholipase D[33] (PLD) and 2-APB to inhibit IP$_3$ (ref. 8). Apocrine secretion evoked via 5-HT$_{2C}$ relied on PLC, PLD and IP$_3$ (Fig. 6f). TRPM3 also led to apocrine secretion but is not a

https://doi.org/10.1038/s41593-025-01972-9

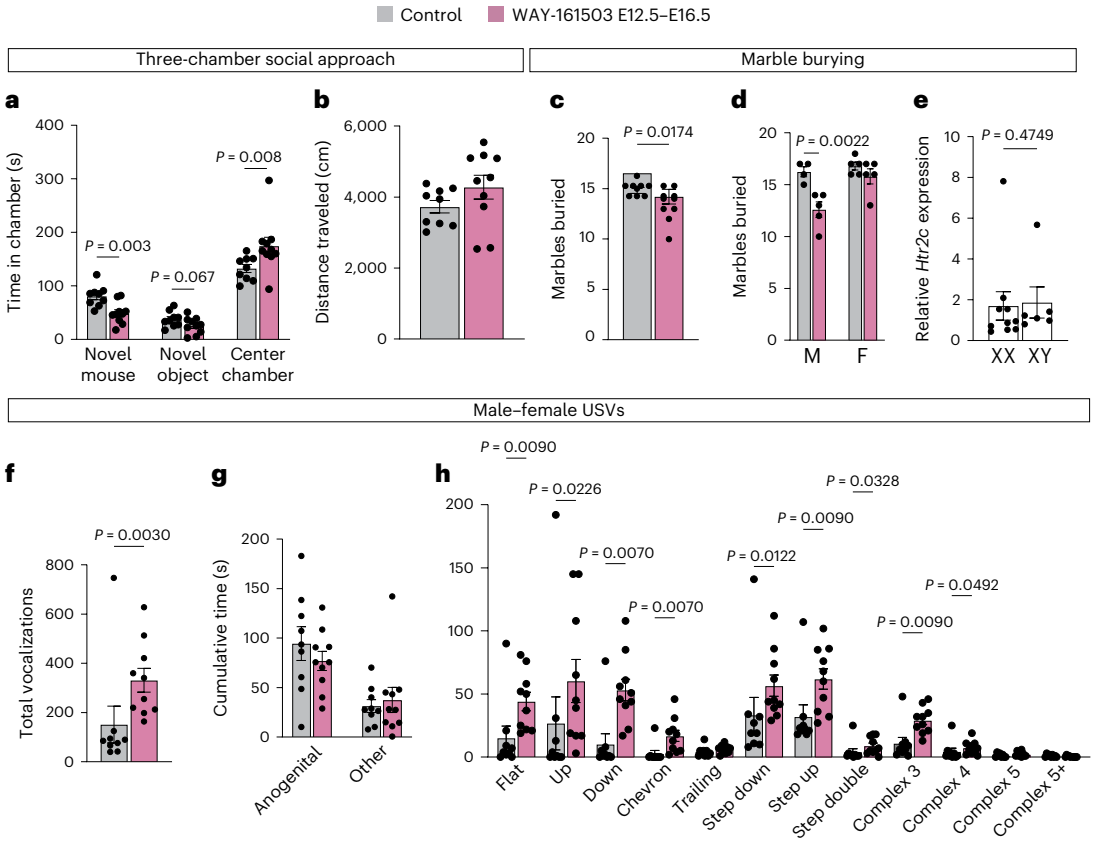

Fig. 5 | Embryonic overstimulation of ChP secretion is associated with abnormal adult behavior. a,**b**, Three-chambered social approach task. The time in the chamber with a novel mouse or novel object or in the center (**a**) and distance traveled (**b**) was assessed (control $N = 9$, WAY-161503 $N = 10$). **c**, Graph of marbles buried (control $N = 9$, WAY-161503 $N = 10$). **d**, Sex differences in marbles buried by control or repeated apocrine mice ($N = 4–5$; male (M) control $N = 4$, WAY-161503 $N = 5$; female (F) control $N = 5$, WAY-161503 $N = 5$). **e**, Relative LV ChP *Htr2c* expression determined by RT–qPCR in E16.5 mice with XY or XX chromosome complement ($N = 7$ XX and 10 XY). **f**,**g**, Male–female USVs. Total vocalizations (**f**) and cumulative time that a male mouse spent in physical contact with a female mouse (**g**) were determined (control $N = 9$, WAY-161503 $N = 10$). **h**, Many subtypes of adult male–female USVs increase after embryonic overstimulation of apocrine secretion (control $N = 9$, WAY-161503 $N = 10$). All data are presented as mean ± s.e.m. *P* values were calculated by one-way ANOVA with a Tukey correction for **a** and **b**, two-tailed *t*-test for **c** and **f**, two-way ANOVA with a Sidak correction for **d** and **h** and Mann–Whitney test for **e** and **g**. All *N* represent the numbers of mice collected from three separate litters.

G-protein-coupled receptor and, as such, did not rely on PLC, PLD, or IP3 (Fig. 6f). However, 5-HT_{2C}- and TRPM3-mediated apocrine secretion were both dependent on the activity of calpains. Calpains are proteases that facilitate Ca^{2+}-mediated cytoskeletal remodeling by cleaving the actin anchor protein ezrin[34]. Inhibition of ChP calpains by preincubation with endogenous protein calpastatin[35] prevented the formation of aposomes after either 5-HT_{2C} or TRPM3 activation (Fig. 6f). However, receptors were still activated, as evidenced by Fos induction (Fig. 6g).

Given that apocrine secretion can be triggered by distinct stimuli that increase intracellular Ca^{2+} levels (such as TRPM3-mediated extracellular Ca^{2+} influx and 5-HT_{2C}-induced release from intracellular stores), we sought to differentiate the roles of intracellular versus extracellular Ca^{2+} sources. Neither increasing extracellular Ca^{2+} concentrations alone nor releasing intracellular Ca^{2+} stores using thapsigargin was sufficient to induce apocrine secretion (Fig. 6h). Moreover, in the absence of extracellular Ca^{2+}, activating 5-HT_{2C} resulted in only a 1.5-fold increase in aposomes compared to a 2.95-fold increase when extracellular Ca^{2+} was available (Fig. 6h). These findings suggest that the combined availability of intracellular and extracellular Ca^{2+} is required to reach the threshold necessary for robust apocrine secretion in ChP epithelial cells.

Apocrine secretion can occur at supraphysiological levels in more naturalistic paradigms. Maternal immune activation (MIA) increases the risk of many neurodevelopmental disorders, can cause cerebral cortical abnormalities[36] and can create an inflammatory signature in the CSF[37]. We modeled MIA using polyinosinic–polycytidylic acid (poly(I:C); Fig. 6i) and examined ChP epithelial cells for aposomes at 24 and 48 h following maternal poly(I:C) administration, revealing more than a fivefold increase in aposomes at 24 h (Fig. 6j). Supraphysiological levels of aposomes were transient, as above-baseline levels were not observed at 48 h. Propagation of MIA to the embryonic brain was apparent by increased ChP immune cells at both time points (Extended Data Fig. 8c). These findings suggest that ChP apocrine secretion may modulate CSF contents during acute inflammation. Collectively, our results demonstrate that apocrine secretion can be evoked through various stimuli with far-reaching consequences for brain development (Fig. 7).

We attempted to distinguish apocrine secretion from other release mechanisms by blocking calpain activity in E16.5 LV ChP explants using calpastatin (Supplementary Fig. 1a). This inhibition selectively reduced the abundance of certain CSF proteins while leaving others unaffected, suggesting that apocrine secretion uniquely contributes to the ChP secretome (Supplementary Fig. 1b–e). Many of the proteins dependent on apocrine release mapped to neuronal development pathways (Supplementary Fig. 1f). However, given the broader effects of calpain inhibition including potentially on other modes of secretion[38,39] and the variability of aptamer-based proteomic detection[40–42], these findings require cautious interpretation.

https://doi.org/10.1038/s41593-025-01972-9

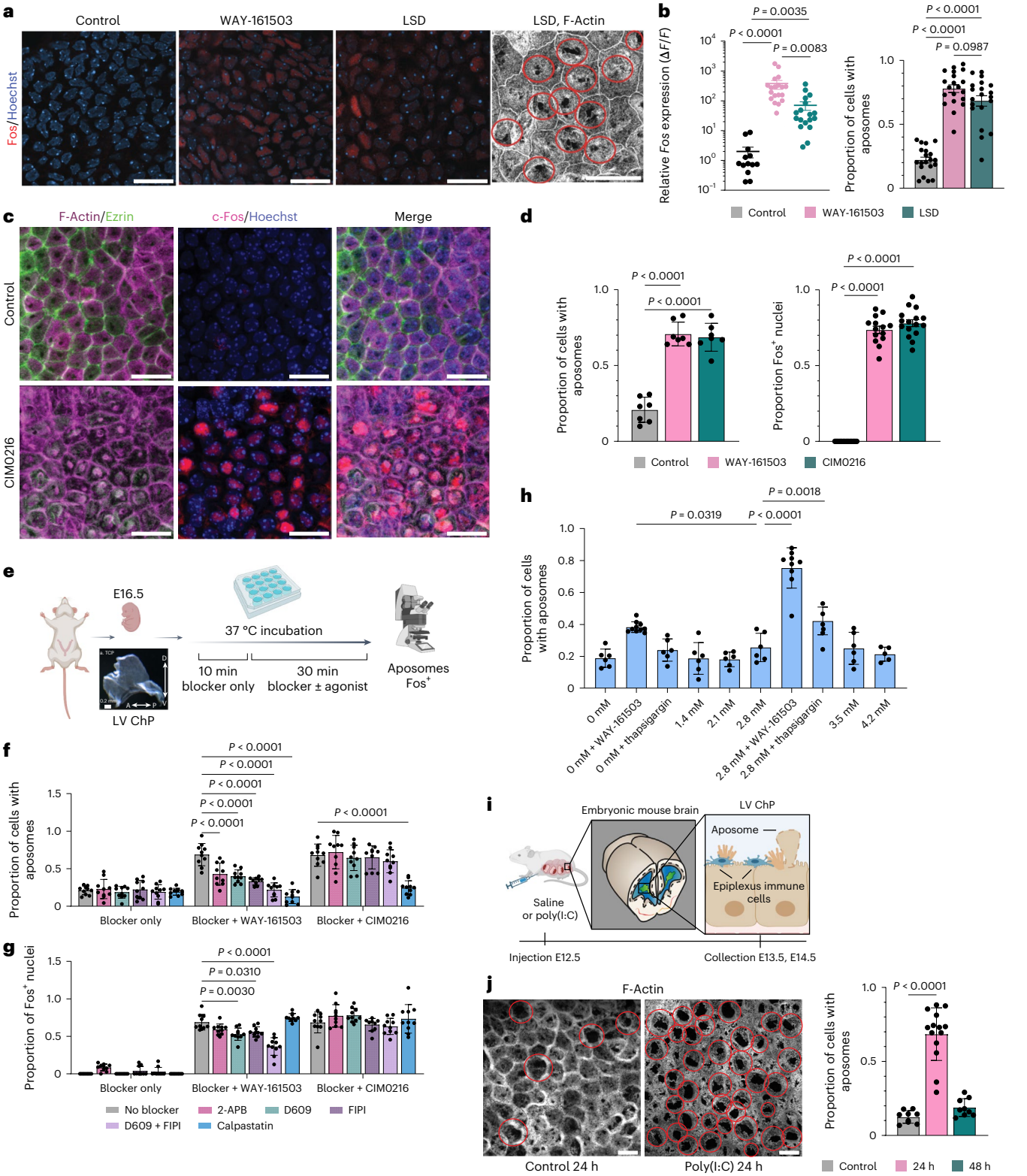

Fig. 6 | An approach for screening maternal–fetal apocrine triggers. **a**, Confocal images of the E16.5 LV ChP; scale bars, 20 µm. **b**, Left: RT–qPCR of *Fos* in the E16.5 ChP (saline $N = 13$, five litters; WAY-161503 $N = 19$, five litters; LSD $N = 18$, five litters). Right: proportion of cells with aposomes in the E16.5 LV ChP after maternal LSD exposure. **c**, Confocal images of the E16.5 LV ChP; scale bars, 20 µm. **d**, Proportion of cells with Fos (right) or aposomes (left) in the E16.5 LV ChP following maternal saline ($N = 7$, three litters), WAY-161503 ($N = 7$, three litters) or CIM0216 ($N = 6$, three litters) injection. **e**, Experiment for results in **f** and **g**. **f**,**g**, Aposomes (**f**) and Fos expression (**g**) in the E16.5 LV ChP after incubation with blockers and agonists; $N = 10$ explants per condition. **h**, Proportion of cells with aposomes after LV ChP incubation with various treatments (0 mM Ca^{2+} $N = 6$, 0 mM Ca^{2+} + WAY-161503 $N = 10$, 0 mM Ca^{2+} + thapsigargin $N = 6$, 1.4 mM Ca^{2+} $N = 6$, 2.1 mM Ca^{2+} $N = 6$, 2.8 mM Ca^{2+} $N = 6$, 2.8 mM Ca^{2+} + WAY-161503 $N = 9$, 2.8 mM Ca^{2+} + thapsigargin $N = 11$, 3.5 mM Ca^{2+} $N = 6$, 4.2 mM Ca^{2+} $N = 5$). **i**, Experimental schematic for results in **j**. **j**, Representative confocal images and quantification of aposomes (circled in red) in the E14.5 LV ChP after maternal saline ($N = 9$) or poly(I:C) injection (24 h $N = 14$, 48 h $N = 9$); scale bar 20 µm. All data are presented as mean ± s.e.m. *P* values were calculated by Kruskal–Wallis test for **a**, **d** and **j** or two-way ANOVA with a Sidak correction for **f**–**h**. Panels **e** and **i** created with BioRender.com.

https://doi.org/10.1038/s41593-025-01972-9

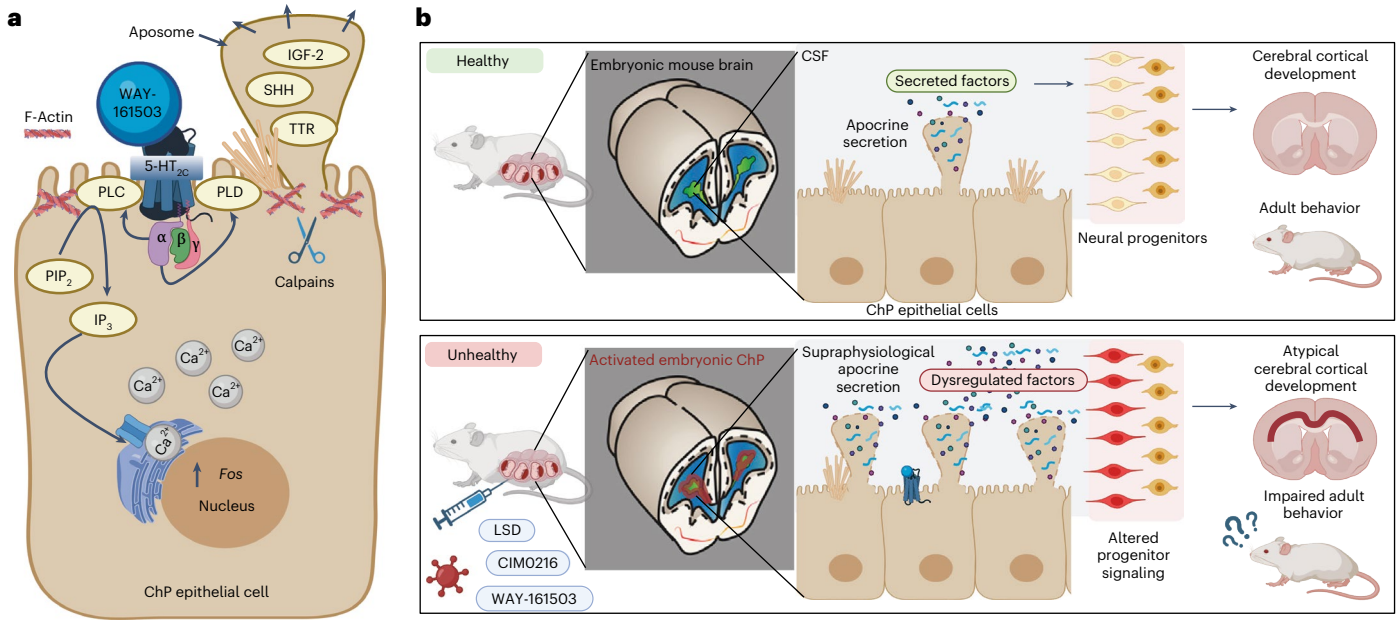

Fig. 7 | Embryonic ChP apocrine secretion mechanism and effects of overstimulation. a, Schematic depicting the intracellular mechanisms of apocrine secretion downstream of 5-HT$_{2C}$ or TRPM3. **b**, Schematic depicting a healthy level of embryonic apocrine secretion versus an unhealthy supraphysiological level and their effects on cerebral cortical development. Figure created with BioRender.com.

Discussion

Our study reveals that the embryonic ChP uses apocrine secretion to shape the CSF environment and, consequently, brain development. Although earlier observations hinted at the possibility of apocrine secretion by the ChP[43], our data clarify and expand on this mechanism. In addition to known secretory modes at the ChP, including exosome release and extracellular vesicles[44–46], our findings establish apocrine secretion as a fundamental process by which the ChP can rapidly alter CSF composition. We demonstrate that activating ChP epithelial cells is associated with alterations in neural progenitor fate, cortical architecture and long-term behavioral outcomes.

We found that embryonic ChP cells respond to maternally administered 5-HT$_{2C}$ agonists, such as WAY-161503, by increasing intracellular Ca^{2+}, inducing immediate early gene expression and secreting proteins into the CSF. This activation and resultant altered CSF milieu was associated with changes in cortical cell populations: reduced deep-layer TBR1^{+} neurons alongside increases in SATB2^{+} neurons, SST^{+} interneurons, astrocytes and microglia. These alterations were accompanied by behavioral changes in adult mice, including social deficits and repetitive behaviors. Although we observed no changes in gross brain morphology or pup weight (Extended Data Fig. 7a–d), we acknowledge that potential anorectic effects of WAY-161503 on the pregnant dam[47] could still have subtle metabolic impacts on development.

These findings extend to other serotonergic agonists, including the psychedelic LSD, a potent 5-HT$_{2C}$ agonist. Given renewed clinical interest in psychedelics, our results highlight the importance of evaluating potential risks during pregnancy, as maternal exposure to such compounds could trigger ChP secretion and thus influence fetal brain development. Beyond serotonergic stimuli, our evidence that TRPM3 channel activation similarly induces ChP apocrine secretion through a calpain-dependent pathway suggests broad sensitivity. Increased intracellular Ca^{2+} (from a range of stimuli) could dysregulate CSF composition. For example, maternal hyperthermia, which could activate the heat-sensitive TRPM3 channels, might offer a mechanistic link to the increased risk of neurodevelopmental disorders associated with fevers during pregnancy.

The apocrine mechanism we describe is reminiscent of secretion observed in other glandular epithelia, including salivary glands[48], mammary glands[49], the prostate[50] and apocrine sweat glands[51]. Like these tissues, the ChP uses apocrine secretion to release large proteinaceous cytosolic portions into a fluid-filled lumen (the CSF). Our findings indicate that embryonic ChP secretion can introduce a range of signaling molecules into the developing brain's extracellular milieu, including angiopoietin-1, NRG1, MIF, ephrin-A5 and PDGFA. Collectively, these factors may modulate multiple developmental pathways, including Wnt, Notch and SHH, to influence neural progenitor proliferation and differentiation and the emergence of distinct cortical cell types. For instance, angiopoietin-1 can promote neural progenitor proliferation and differentiation through the Notch and Wnt signaling pathways[52]. Similarly, NRG1 is a well-known extrinsic signal for progenitor proliferation, differentiation[53] and migration[54], whereas MIF has been implicated in maintaining stemness by upregulating SOX6 (ref. 55). Ephrin-A5 signaling has been linked to upper-layer neuron production[56], and PDGFA contributes to astroglial proliferation and differentiation[57,58]. Although the current study documents these shifts in protein abundance, future work is needed to establish the precise mechanism by which each factor acts on cortical progenitors during development.

Our findings indicate that both apocrine and vesicular pathways contribute to the embryonic ChP secretome, but parsing their specific roles remains challenging. Although we attempted to selectively block apocrine release by inhibiting calpain, this approach may also diminish vesicular secretion. We considered the use of brefeldin A or monensin to instead inhibit vesicular exocytosis, but these agents disrupt the Golgi apparatus, have broad effects on protein trafficking and may also interfere with apocrine processes[49,59]. Indeed, brefeldin A largely abolishes apical milk protein secretion in mammary epithelial cells[60,61], and a recent preprint indicates that it blocks TTR secretion[62], a protein we identify as apocrine cargo. Monensin similarly inhibits milk protein release[63] and secretion from the apocrine coagulating gland[64]. Thus, implementing these tools would require extensive optimization to avoid confounding impacts on both secretory modes. In line with these complexities, a previous analysis of ChP cell cultures treated with brefeldin A concluded that many proteins were vesicle derived[65], yet our calpastatin experiments suggest that some of the same proteins may be released in aposomes (or partially inhibited by calpastatin), underscoring the overlap between these pathways. Ultimately, a thorough,

mechanistic dissection of apocrine versus vesicular cargo will require identifying new inhibitors or gene-editing strategies that eliminate off-target effects, enabling a more precise understanding of how ChP cells regulate embryonic CSF composition.

To our knowledge, no prior studies have investigated how CSF-borne signals influence neural progenitor fate in the MGE and LGE, regions critical for generating diverse neuronal subtypes. Our findings reveal the possibility that ChP-secreted factors, which impact cerebral cortical progenitors, also shape ventral progenitor dynamics, introducing questions about how regional differences in receptor expression, CSF flow and/or protein distribution influence brain development. This conceptual extension broadens the role of CSF signaling across brain regions and highlights its potential relevance to cell types arising from the MGE and LGE, including cortical interneurons, striatal projection neurons and other subcortical populations. CSF signals can also act in hindbrain development[66], insulin delivered into the third ventricle can modulate hypothalamic circuits[67], and adult neural stem cells respond to CSF-derived cues[1,46]. Collectively, these findings suggest that CSF-borne factors influence multiple brain regions and developmental stages, supporting a broad, long-range role for CSF signaling in neurodevelopment and homeostasis.

Our study provides evidence that ChP apocrine secretion alters the CSF proteome and influences brain development, yet several limitations warrant consideration. Although we demonstrate changes in neural progenitor dynamics and cortical architecture following ChP overstimulation, we acknowledge that the mechanistic link(s) between these developmental alterations and the observed behavioral abnormalities in adult animals are not resolved. Specifically, we have not mechanistically addressed how WAY-161503-induced ChP secretion directly leads to the behavioral changes observed, and it is likely that these outcomes involve broader and more complex disruptions beyond the phenotypes we have characterized. Future studies are needed to determine whether long-lasting changes in embryonic progenitor proliferation and differentiation are restricted to the cerebral cortex or extend to subcortical regions, such as those that originate from the MGE and LGE, where progenitor-derived cell types may also contribute to long-term behavioral effects.

Our findings also emphasize the importance of considering how maternal anesthesia affects embryonic brain activity. Although Yuryev et al. reported that maternal isofluorane does not alter frontal cortex neuronal activity and that ketamine inhibits it[68], and Munz et al. found no impact of isofluorane or fentanyl/medetomidine/midazolam anesthesia on spontaneous embryonic neuronal Ca^{2+} activity[15], we observed that maternal isoflurane inhibits ChP epithelial cell activity and that urethane/ketamine only modestly decreases it. These differences suggest that the embryonic brain's response to maternal anesthetic exposure may vary depending on both the type of anesthetic used and the specific cell population examined.

In conclusion, our study establishes ChP apocrine secretion as a key regulator of the developing neural environment, one that can be rapidly influenced by maternal physiology and external stimuli. This mode of secretion alters CSF composition and is associated with changes in progenitor fate, cerebral cortical architecture and long-term behavioral outcomes. Understanding this system opens avenues for mitigating adverse prenatal exposures and harnessing the ChP's intrinsic secretory capabilities for therapeutic benefit. Beyond embryonic development, ChP apocrine secretion persists in adult mice and can be triggered by the same stimuli. Apocrine secretion may thus play a life-long role in ChP–CSF signaling in health and disease.

Online content

Any methods, additional references, Nature Portfolio reporting summaries, source data, extended data, supplementary information, acknowledgements, peer review information; details of author contributions and competing interests; and statements of data and code availability are available at https://doi.org/10.1038/s41593-025-01972-9.

References

1. Silva-Vargas, V., Maldonado-Soto, A. R., Mizrak, D., Codega, P. & Doetsch, F. Age-dependent niche signals from the choroid plexus regulate adult neural stem cells. *Cell Stem Cell* **19**, 643–652 (2016).
2. Saunders, N. R., Dziegielewska, K. M., Fame, R. M., Lehtinen, M. K. & Liddelow, S. A. The choroid plexus: a missing link in our understanding of brain development and function. *Physiol. Rev.* **103**, 919–956 (2023).
3. Damkier, H. H., Brown, P. D. & Praetorius, J. Cerebrospinal fluid secretion by the choroid plexus. *Physiol. Rev.* **93**, 1847–1892 (2013).
4. Lun, M. P. et al. Spatially heterogeneous choroid plexus transcriptomes encode positional identity and contribute to regional CSF production. *J. Neurosci.* **35**, 4903–4916 (2015).
5. Lehtinen, M. K. et al. The cerebrospinal fluid provides a proliferative niche for neural progenitor cells. *Neuron* **69**, 893–905 (2011).
6. Watson, J. A., Elliott, A. C. & Brown, P. D. Serotonin elevates intracellular Ca^{2+} in rat choroid plexus epithelial cells by acting on 5-HT_{2C} receptors. *Cell Calcium* **17**, 120–128 (1995).
7. Esterle, T. M. & Sanders-Bush, E. Serotonin agonists increase transferrin levels via activation of 5-HT_{1C} receptors in choroid plexus epithelium. *J. Neurosci.* **12**, 4775–4782 (1992).
8. Mazucanti, C. H. et al. Release of insulin produced by the choroids plexis is regulated by serotonergic signaling. *JCI Insight* **4**, e131682 (2019).
9. Rosenzweig-Lipson, S. et al. Antiobesity-like effects of the 5-HT_{2C} receptor agonist WAY-161503. *Brain Res.* **1073–1074**, 240–251 (2006).
10. Shipley, F. B. et al. Tracking calcium dynamics and immune surveillance at the choroid plexus blood–cerebrospinal fluid interface. *Neuron* **108**, 623–639 (2020).
11. Dani, N. et al. A cellular and spatial map of the choroid plexus across brain ventricles and ages. *Cell* **184**, 3056–3074 (2021).
12. Farkaš, R. Apocrine secretion: new insights into an old phenomenon. *Biochim. Biophys. Acta* **1850**, 1740–1750 (2015).
13. Madisen, L. et al. Transgenic mice for intersectional targeting of neural sensors and effectors with high specificity and performance. *Neuron* **85**, 942–958 (2015).
14. Zhang, Y. et al. A transgenic *FOXJ1-cre* system for gene inactivation in ciliated epithelial cells. *Am. J. Respir. Cell Mol. Biol.* **36**, 515–519 (2007).
15. Munz, M. et al. Pyramidal neurons form active, transient, multilayered circuits perturbed by autism-associated mutations at the inception of neocortex. *Cell* **186**, 1930–1949 (2023).
16. Woodworth, M. B., Greig, L. C., Kriegstein, A. R. & Macklis, J. D. SnapShot: cortical development. *Cell* **151**, https://doi.org/10.1016/j.cell.2012.10.004 (2012).
17. Lun, M. P., Monuki, E. S. & Lehtinen, M. K. Development and functions of the choroid plexus-cerebrospinal fluid system. *Nat. Rev. Neurosci.* **16**, 445–457 (2015).
18. Loo, L. et al. Single-cell transcriptomic analysis of mouse neocortical development. *Nat. Commun.* **10**, 134 (2019).
19. Russell, A. J. C. et al. Slide-tags enables single-nucleus barcoding for multimodal spatial genomics. *Nature* **625**, 101–109 (2023).
20. Di Bella, D. J. et al. Molecular logic of cellular diversification in the mouse cerebral cortex. *Nature* **595**, 554–559 (2021).
21. Asano, S. M. et al. Expansion microscopy: protocols for imaging proteins and RNA in cells and tissues. *Curr. Protoc. Cell Biol.* **80**, e56 (2018).
22. Alshehri, B., D'Souza, D. G., Lee, J. Y., Petratos, S. & Richardson, S. J. The diversity of mechanisms influenced by transthyretin in neurobiology: development, disease and endocrine disruption. *J. Neuroendocrinol.* **27**, 303–323 (2015).

23. Yang, A. C. et al. Dysregulation of brain and choroid plexus cell types in severe COVID-19. *Nature* **595**, 565–571 (2021).
24. Farkaš, R. et al. Apocrine secretion in *Drosophila* salivary glands: subcellular origin, dynamics, and identification of secretory proteins. *PLoS ONE* **9**, e94383 (2014).
25. Ohsawa, S., Vaughen, J. & Igaki, T. Cell extrusion: a stress-responsive force for good or evil in epithelial homeostasis. *Dev. Cell* **44**, 284–296 (2018).
26. Gold, L. et al. Aptamer-based multiplexed proteomic technology for biomarker discovery. *PLoS ONE* **5**, e15004 (2010).
27. Coulter, M. E. et al. The ESCRT-III protein CHMP1A mediates secretion of sonic hedgehog on a distinctive subtype of extracellular vesicles. *Cell Rep.* **24**, 973–986 (2018).
28. Ray, T. S. Psychedelics and the human receptorome. *PLoS ONE* **5**, e9019 (2010).
29. Sanders-Bush, E., Burris, K. D. & Knoth, K. Lysergic acid diethylamide and 2,5-dimethoxy-4-methylamphetamine are partial agonists at serotonin receptors linked to phosphoinositide hydrolysis. *J. Pharmacol. Exp. Ther.* **246**, 924–928 (1988).
30. Xu, Y. et al. 5-HT_{2C}Rs expressed by pro-opiomelanocortin neurons regulate energy homeostasis. *Neuron* **60**, 582–589 (2008).
31. Held, K. et al. Activation of TRPM3 by a potent synthetic ligand reveals a role in peptide release. *Proc. Natl Acad. Sci. USA* **112**, E1363–E1372 (2015).
32. Kalluri, H. S. G. & Dempsey, R. J. D609-mediated inhibition of ATP synthesis in neural progenitor cells. *Neuroreport* **25**, 777–781 (2014).
33. Tanguy, E. et al. Mono- and poly-unsaturated phosphatidic acid regulate distinct steps of regulated exocytosis in neuroendocrine cells. *Cell Rep.* **32**, 108026 (2020).
34. Potter, D. A. et al. Calpain regulates actin remodeling during cell spreading. *J. Cell Biol.* **141**, 647–662 (1998).
35. Huang, L., Kutluer, M., Adani, E., Comitato, A. & Marigo, V. New in vitro cellular model for molecular studies of retinitis pigmentosa. *Int. J. Mol. Sci.* **22**, 6440 (2021).
36. Choi, G. B. et al. The maternal interleukin-17A pathway in mice promotes autism-like phenotypes in offspring. *Science* **351**, 933–939 (2016).
37. Cui, J. et al. Inflammation of the embryonic choroid plexus barrier following maternal immune activation. *Dev. Cell* **55**, 617–628 (2020).
38. Evans, J. S. & Turner, M. D. Emerging functions of the calpain superfamily of cysteine proteases in neuroendocrine secretory pathways. *J. Neurochem.* **103**, 849–859 (2007).
39. Williams, J. K. et al. Calpains orchestrate secretion of annexin-containing microvesicles during membrane repair. Preprint at *bioRxiv* https://doi.org/10.1101/2024.09.05.611512 (2024).
40. Candia, J., Daya, G. N., Tanaka, T., Ferrucci, L. & Walker, K. A. Assessment of variability in the plasma 7k SomaScan proteomics assay. *Sci. Rep.* **12**, 17147 (2022).
41. Joshi, A. & Mayr, M. In aptamers they trust: the caveats of the SomaScan biomarker discovery platform from SomaLogic. *Circulation* **138**, 2482–2485 (2018).
42. Haslam, D. E. et al. Stability and reproducibility of proteomic profiles in epidemiological studies: comparing the Olink and SomaScan platforms. *Proteomics* **22**, e2100170 (2022).
43. Agnew, W. F., Yuen, T. G. & Achtyl, T. R. Ultrastructural observations suggesting apocrine secretion in the choroid plexus: a comparative study. *Neurol. Res* **1**, 313–332 (1980).
44. Balusu, S. et al. Identification of a novel mechanism of blood–brain communication during peripheral inflammation via choroid plexus-derived extracellular vesicles. *EMBO Mol. Med.* **8**, 1162–1183 (2016).
45. Feliciano, D. M., Zhang, S., Nasrallah, C. M., Lisgo, S. N. & Bordey, A. Embryonic cerebrospinal fluid nanovesicles carry evolutionarily conserved molecules and promote neural stem cell amplification. *PLoS ONE* **9**, e88810 (2014).
46. Ditte, Z., Silbern, I., Ditte, P., Urlaub, H. & Eichele, G. Extracellular vesicles derived from the choroid plexus trigger the differentiation of neural stem cells. *J. Extracell. Vesicles* **11**, e12276 (2022).
47. Garfield, A. S. et al. Increased alternate splicing of *Htr2c* in a mouse model for Prader–Willi syndrome leads disruption of 5-HT_{2C} receptor mediated appetite. *Mol. Brain* **9**, 95 (2016).
48. Babišová, K. et al. Apocrine secretion in the salivary glands of Drosophilidae and other dipterans is evolutionarily conserved. *Front. Cell Dev. Biol.* **10**, 1088055 (2022).
49. Monks, J. et al. Perilipin-2 promotes lipid droplet–plasma membrane interactions that facilitate apocrine lipid secretion in secretory epithelial cells of the mouse mammary gland. *Front. Cell Dev. Biol.* **10**, 958566 (2022).
50. Fullwood, N. J., Lawlor, A. J., Martin-Hirsch, P. L., Matanhelia, S. S. & Martin, F. L. An analysis of benign human prostate offers insights into the mechanism of apocrine secretion and the origin of prostasomes. *Sci. Rep.* **9**, 4582 (2019).
51. Li, S. et al. Defining key genes regulating morphogenesis of apocrine sweat gland in sheepskin. *Front. Genet.* **10**, 739 (2019).
52. Rosa, A. I. et al. The angiogenic factor angiopoietin-1 is a proneurogenic peptide on subventricular zone stem/progenitor cells. *J. Neurosci.* **30**, 4573–4584 (2010).
53. Sato, T. et al. Neuregulin 1 type II–ErbB signaling promotes cell divisions generating neurons from neural progenitor cells in the developing zebrafish brain. *PLoS ONE* **10**, e0127360 (2015).
54. Fornasari, B. E. et al. Neuregulin1 α activates migration of neuronal progenitors expressing ErbB4. *Mol. Cell. Neurosci.* **77**, 87–94 (2016).
55. Ohta, S. et al. *Sox6* up-regulation by macrophage migration inhibitory factor promotes survival and maintenance of mouse neural stem/progenitor cells. *PLoS ONE* **8**, e74315 (2013).
56. Gerstmann, K. et al. Thalamic afferents influence cortical progenitors via ephrin A5–EphA4 interactions. *Development* **142**, 140–150 (2015).
57. Singh, J., Sharma, K., Frost, E. E. & Pillai, P. P. Role of PDGF-A-activated ERK signaling mediated FAK–paxillin interaction in oligodendrocyte progenitor cell migration. *J. Mol. Neurosci.* **67**, 564–573 (2019).
58. Dai, C. et al. PDGF autocrine stimulation dedifferentiates cultured astrocytes and induces oligodendrogliomas and oligoastrocytomas from neural progenitors and astrocytes in vivo. *Genes Dev.* **15**, 1913–1925 (2001).
59. Klausner, R. D., Donaldson, J. G. & Lippincott-Schwartz, J. Brefeldin A: insights into the control of membrane traffic and organelle structure. *J. Cell Biol.* **116**, 1071–1080 (1992).
60. Lkhider, M., Castino, R., Bouguyon, E., Isidoro, C. & Ollivier-Bousquet, M. Cathepsin D released by lactating rat mammary epithelial cells is involved in prolactin cleavage under physiological conditions. *J. Cell Sci.* **117**, 5155–5164 (2004).
61. Pauloin, A. et al. Brefeldin A differently affects basal and prolactin-stimulated milk protein secretion in lactating rabbit mammary epithelial cells. *Eur. J. Cell Biol.* **72**, 324–336 (1997).
62. Masters, H. et al. Sequential emergence and contraction of epithelial subtypes in the prenatal human choroid plexus revealed by a stem cell model. Preprint at *bioRxiv* https://doi.org/10.1101/2024.06.12.598747 (2024).
63. Ollivier-Bousquet, M. & Ahmed-Ali, M. Effects of monensin on the secretion of caseins by mammary epithelial cells from lactating rabbits. *Reprod. Nutr. Dev.* **28**, 303–317 (1988).

64. Bartlett, R. J., French, F. S. & Wilson, E. M. In vitro synthesis and glycosylation of androgen-dependent secretory proteins of rat dorsal prostate and coagulating gland. *Prostate* **5**, 75–91 (1984).
65. Thouvenot, E. et al. The proteomic analysis of mouse choroid plexus secretome reveals a high protein secretion capacity of choroidal epithelial cells. *Proteomics* **6**, 5941–5952 (2006).
66. Kaiser, K. et al. WNT5A is transported via lipoprotein particles in the cerebrospinal fluid to regulate hindbrain morphogenesis. *Nat. Commun.* **10**, 1498 (2019).
67. Mazucanti, C. H. et al. AAV5-mediated manipulation of insulin expression in choroid plexus has long-term metabolic and behavioral consequences. *Cell Rep.* **42**, 112903 (2023).
68. Yuryev, M. et al. In vivo two-photon imaging of the embryonic cortex reveals spontaneous ketamine-sensitive calcium activity. *Sci. Rep.* **8**, 16059 (2018).
69. Byer, L. I. J., Xu, H. & Lehtinen, M. K. Protocol for the dissection, immunostaining, and imaging of whole-mount mouse choroid plexus. *STAR Protoc.* **6**, 103627 (2025).

Methods

Ethical regulations

Our research complies with all relevant ethical regulations. The Boston Children's Hospital Institutional Animal Care and Use Committee approved all mouse studies as per protocols 00002094 and 00002095. Deidentified second-trimester ChP tissue samples were collected from induced pregnancy-termination specimens at the University of California Davis Medical Center. The samples were acquired with consent stating that tissues removed as part of the procedure may be used anonymously for research, as permitted by federal and state law. Individuals were provided with information about this option only after they had decided to terminate the pregnancy and had reviewed the risk of the procedure, ensuring that the decision to terminate was not influenced by the option to donate. In strict observance of legal and institutional ethical regulations, participants were not recruited, were not compensated and were not provided any incentives for donation. There were no additional medical risks associated with tissue donation, and participants received the same hospital care regardless of their decision about donation. The obstetricians that obtained participant consent were not involved in the study and did not alter the timing, method or procedure used to terminate the pregnancy. All research protocols were reviewed and approved by the Institutional Review Board at the University of California, Davis (2194800-1).

Mice

Animals were housed in a temperature- and humidity-controlled room (21 ± 1.5 °C, 35–70% humidity) on a 12-h light/12-h dark cycle (7 a.m. on 7 p.m. off) and had free access to food and water. We used equal numbers of male and female mice unless otherwise stated. Adult and timed-pregnant mice were obtained from Charles River Laboratories or The Jackson Laboratory or were bred in-house.

Resource	Source	Identifier
Mouse: C57/BL6	Bred in-house or obtained from Charles River Laboratories	RRID:MGI:7264769
Mouse: CD-1	Bred in-house or obtained from Charles River Laboratories	RRID:MGI:5649524
Mouse: B6.129-*Htr2c*^{tm1Jke}/J	Gifted from J. Elmquist (University of Texas Southwestern) and bred in-house	RRID:IMSR_JAX:015821
Mouse: *FoxJ1-cre* (C57/BL6 background)	Ref. 14	N/A
Mouse: *Ai95D* (RCL-GCaMP6f)-D (C57/BL6 background)	The Jackson Laboratory	RRID:IMSR_JAX:028865

Behavioral analyses

Behavioral analyses were performed using CD-1 mice, ten mice per condition, beginning at age P90, in collaboration with the Boston Children's Hospital Animal Behavior and Physiology Core.

Three-chamber social approach. Methods were closely based on previous publications[70–72]. The testing apparatus (a rectangular three-chambered box, 40 × 60 × 23 cm fabricated from matte white acrylic (P95 White, Tap Plastics)) was Illuminated by an infrared light source (Nightvisionexperts.com). Mice could move between chambers (5 × 10 cm) through opaque retractable doors (12 × 33 cm). Mouse activity was detected by a top-mounted infrared-sensitive camera (Ikegami ICD-49, B&H Photo) and analyzed with Noldus EthoVision XT videotracking software (version 9.0, Noldus Information Technologies). Software-defined zones included each chamber as well as an annulus extending 2 cm from each novel object or novel mouse enclosure (inverted wire cup, Galaxy stainless steel pencil and utility cup, Kitchen Plus). Sniff scoring required head direction toward the target.

For habituation and to assess innate side preference, each mouse was placed in the center chamber and allowed to explore all three empty chambers for 10 min. Following this habituation session, a novel object was placed in one side chamber, a novel mouse was placed in the other side chamber, and the test mouse was placed in the center. Novel (129Sv/ImJ) mice were 10–14 weeks old and sex matched. General exploratory locomotion behavior was quantified by number of entries into the side chambers. Sociability was defined as relative time in the chambers with the novel mouse versus the novel object and relative time sniffing the novel mouse versus the novel object.

Male–female USVs. Testing took place in a 33 × 15 × 14 cm plastic cage with 3 cm of sawdust and a metal flat cover. Male mice were habituated for 30 min. An unfamiliar female mouse (an adult Naval Medical Research Institute outbred mouse line, different for each tested male) was then placed into the testing cage for 3 min. Previous studies have shown that in these experimental settings, USVs are emitted only by the male mouse in the male–female interaction[73,74]. Spectrograms were inspected to exclude the presence of 'double calls', that is, overlapping in time but with different, nonharmonic characteristics (for example, different peak and mean frequency), which would indicate the concomitant emission of USVs by the two interacting mice during testing.

Video recordings from a camera placed on the side of the cage were analyzed with Observer XT (Noldus). One observer who was unaware of the genotype and stress conditions of the animals quantified the time each male mouse spent performing affiliative behaviors[75–77], that is, sniffing the head and the snout of the partner, its anogenital region or any other body part or contact with a partner such as crawling over/under the partner's body or allogrooming. Nonsocial activities measured included rearing (standing on the hind limbs sometimes with the forelimbs against the walls of the cage), digging and self-grooming (licking and mouthing its own fur). An ultrasonic microphone UltraSoundGate Condenser Microphone CM 16 (Avisoft Bioacoustics) mounted 2 cm above the cover of the testing cage was connected via an UltraSoundGate 116 USB audio device (Avisoft Bioacoustics) to a computer, where acoustic data were recorded with a sampling rate of 250 kHz in 16-bit format by Avisoft Recorder (version 2.97; Avisoft Bioacoustics).

Recordings were analyzed with Sonotrack Call Classification Software (version 1.4.7, Metris), which recognizes different USV types and calculates quantitative parameters, including the total number and mean duration of the calls. Based on previously reported USV call types[78–80], we selected to quantify short, flat, (ramp) up, (ramp) down, chevron, step up, step down, step double (split), complex 3, complex 4, complex 5 and complex 5+.

Marble burying. Testing was conducted in the presence of white noise (55 dB) and a light intensity of 30 lx. Clean cages (27 × 16.5 × 12.5 cm) were filled with 4.5-cm corncob bedding overlayed with 20 black glass marbles (15 mm in diameter) equidistant in a 4 × 5 arrangement. Mice were placed in these cages for 30 min, and we counted the total number of marbles buried (>66% of the marble covered by bedding material).

ChP dissection

The LV was exposed by separating the cerebral cortical hemispheres. The hippocampus was freed and gently rolled out of the ventricle to expose the underlying LV ChP. The 3V ChP, identifiable by a blood vessel running along its rostro–caudal axis, was approached from the dorsal midbrain. The 4V ChP was exposed by gently moving aside the cerebellum overlying the cisterna magna.

ChP explant/whole-mount culture and blocker treatments

ChP explants were rapidly, completely and cleanly microdissected from E16.5 CD-1 mouse brains, separated by ventricle (LV, 3V and 4V) and maintained in oxygenated aCSF at 37 °C. For ELISA experiments, five embryonic explants per well were placed in 50 µl of aCSF in a 96-well plate. After explant treatment with bath-applied 5 µM WAY-161503 (5-HT_{2C} agonist) or vehicle control (0.9% saline) for 30 min, conditioned aCSF was collected, flash-frozen on dry ice and stored at −80 °C. Recombinant human calpastatin peptide (Abcam, ab157532) was dissolved in sterile water to a stock concentration of 1 mM. ChP explants were preincubated with 10 µM calpastatin in aCSF for 10 min. WAY-161503 (5 µM) was then added, and explants were further incubated for 30 min. ChP explants were preincubated with the following blockers for 10 min before the addition of 5 µM WAY-161503 (5-HT_{2C} agonist; Tocris, 1801) or CIM0216 (TRPM3 agonist; Tocris, 5521) for an additional 30 min: D609 (phosphatidylcholine-specific PLC inhibitor; R&D Systems, 1437) at 100 µM in DMSO, FIPI (PLD inhibitor; R&D Systems, 3600) at 500 nM in DMSO and 2-APB (IP_3 receptor antagonist; R&D Systems, 1224) at 100 µM in DMSO. Vehicle controls contained equivalent concentrations of DMSO.

To assess aposomes and immediate early gene expression, explants were fixed for immunohistochemistry or electron microscopy (as described below). For Ca^{2+} concentration experiments, explants were placed in aCSF with varying Ca^{2+} concentrations immediately after dissection and incubated for 10 min at 37 °C, followed by the addition of WAY-161503, thapsigargin (10 mM; Millipore Sigma, 568006) or vehicle. After a 30-min incubation, explants were processed for immunostaining.

Within 30 min of surgical removal, human ChP specimens were dissected in HBSS buffer, cooled on ice, transferred to an incubator and acclimated in aCSF. ChP tissue sections (~1 ×1 mm) were then incubated with or without 0.5 or 5 µM WAY-161503 in 50 µl of aCSF for 1 h at 37 °C and 5% CO_2, followed by immediate fixation in 4% paraformaldehyde (PFA).

In vivo drug delivery

Timed-pregnant CD-1, C57BL/6J or HTr2cLSL/y female mice were injected subcutaneously with WAY-161503 (3 mg per kg (body weight); 10 mM in a volume of 1 µl per g (mouse body weight); Tocris, 1801), CIM0216 (4 mg per kg (body weight); 10 mM in 1.15 µl per g (mouse body weight); Tocris, 5521) or (+)-lysergic acid diethylamide tartrate (0.2 mg per kg (body weight); 0.6 mM in 0.4 µl per g (mouse body weight); NIDA Drug Supply Program, NIDA 7315-004c).

EdU labeling and detection

Timed-pregnant CD-1 mice received a single i.p. injection of EdU (50 mg per kg (body weight); Thermo Fisher Scientific, A10044). EdU was dissolved in sterile 0.9% saline and administered at E12.5 (10:30 a.m.). For experiments involving a single induction of ChP secretion, pregnant dams received an i.p. injection of WAY-161503 (3 mg per kg (body weight)) or vehicle control (0.9% saline) at 10:00 a.m., 30 min before EdU administration.

For embryonic analyses of the cortex and ganglionic eminences, embryos were collected either 2 (12:30 p.m.) or 18 h (3:30 a.m.) following maternal EdU administration. Embryonic heads were drop-fixed in 4% PFA for 2 h and cryoprotected in 30% sucrose in PBS at 4 °C until they sank. Heads were then embedded in OCT compound (Tissue-Tek) and frozen on dry ice. Coronal cryosections were cut at 14 µm thickness using a Leica CM1950 cryostat and mounted on Superfrost Plus microscope slides (Thermo Fisher Scientific).

For postnatal analyses of the S1, mice were killed at P8, and brains were perfusion-fixed with 4% PFA in PBS and drop-fixed overnight at 4 °C. After fixation, brains were cryoprotected in 30% sucrose in PBS at 4 °C until they sank. Brains were then embedded in OCT compound (Tissue-Tek) and frozen on dry ice. Coronal cryosections were cut at 14 µm thickness using a Leica CM1950 cryostat and mounted on Superfrost Plus microscope slides (Thermo Fisher Scientific).

EdU detection was performed using the Click-iT EdU Cell Proliferation Kit for Imaging, Alexa Fluor 488 dye (Invitrogen, C10337) according to the manufacturer's protocol. Briefly, sections were permeabilized with 0.5% Triton X-100 in PBS for 20 min at room temperature. Click-iT reaction cocktail was prepared as per the manufacturer's instructions and applied to sections for 30 min at room temperature, protected from light. Sections were washed in PBS and immunostained for neuronal markers as described below.

ELISAs

ELISAs were performed on age-matched aCSF[81] that was flash-frozen on dry ice and stored at −80 °C after collection. For mouse samples, IGF-2 was measured with an R&D Systems Mouse/Rat/Porcine/Canine IGF-II/IGF2 Quantikine ELISA kit (MG200). For human samples, IGF-2 was measured with an R&D Systems Human IGF-II/IGF2 ELISA kit, Quantikine (DG200). SHH was measured with an R&D Systems Mouse Sonic Hedgehog/Shh N-Terminus Quantikine ELISA kit (MSHH00). Insulin was measured with a Mercodia Ultrasensitive Mouse Insulin ELISA kit (10-1249-01).

H&E staining

Sections (5 µm) from paraffin-embedded CD-1 mouse brains were deparaffinized in xylene and rehydrated via successive incubations in 100% ethanol, 95% ethanol and water. Sections were incubated in Gill 3 hematoxylin (Sigma Aldrich) for 2 min, followed by a 5-s incubation in 0.5% ammonia water to increase the contrast of the hematoxylin stain. Next, sections were rinsed in water and incubated in 1% alcoholic eosin for 3 min. Finally, sections were dehydrated via successive incubations in 95% ethanol and 100% ethanol and mounted onto glass slides with Permount (Thermo Fisher Scientific).

Image acquisition and quantification

Images were acquired with a Zeiss LSM710 or LSM980 microscope at the Boston Children's Hospital Cellular Imaging Core. Images of ChP explants and brain sections were acquired using a ×20 air or ×63 oil objective. Images of ChP explants prepared for protein-retention expansion microscopy were acquired with a ×63/1.2-NA water immersion objective. ZEN Black software was used for image acquisition, and ZEN Blue software was used for Airy processing.

Aposome quantification. Aposome quantification was performed by hand by Y.C. In brief, four ×20 fields of view per ChP explant were acquired, and epithelial cells displaying apocrine structures were counted via either SEM or immunostaining. The proportion of cells with apocrine structures was quantified as the number of epithelial cells with an apocrine protrusion divided by the total number of visible epithelial cells. The proportion of cells with apocrine structures for each of the four fields of view was then averaged and used as $N = 1$ biological replicate per CD-1, C57BL/6J or HTr2cLSL embryo.

c-Fos/Fos^+ nucleus quantification. Fos quantification was performed with ImageJ/FIJI. Four ×20 fields of view were taken per ChP explant, and the average proportion of Fos^+ nuclei in these four fields of view was used as $N = 1$ biological replicate per CD-1, C57BL/6J or HTr2cLSL embryo. Each field of view was thresholded, and the 'Analyze particles' function was used with a size discrimination of over 200 pixels. Counting was performed for Fos channels and DAPI channels, and the number of Fos^+ nuclei was divided by the total number of nuclei to obtain the 'Proportion of Fos^+ nuclei'.

EdU quantification (2 and 18 h). EdU quantification in the embryonic cortex, MGE and LGE of CD-1 mice was performed in QuPath-0.5.1 (ref. 82). Images were acquired on an LSM980 microscope at the

Boston Children's Hospital Cellular Imaging Core using a ×20 air objective. Resulting .czi files were imported into QuPath for analysis. Annotations were drawn over the region of interest as indicated in Fig. 4b. The Cell Detection tool was used to quantify EdU^+ cells per 10,000 μm^2 with the following parameters: detection channel AF488-T3, requested pixel size 0.5 µm, background radius 5 µm, use opening by reconstruction, median filter radius 0.5 µm, sigma 1.5 µm, minimum area 10 μm^2, maximum area 100 μm^2, threshold 400, split by shape, cell expansion 11.6138 µm, include cell nucleus, smooth boundaries, make measurements.

Excitatory neuronal marker counting and coexpression analysis. Cerebral cortical layer marker counting and colocalization was performed using Biodock software[83] for CD-1 and C57BL/6J mice. A fully automated artificial intelligence (AI) model was trained by a three-step iterative process on three test staining images containing CTIP2, SATB2, TBR1 and DAPI. Input images were four channels. TIF files were obtained by importing the .czi file from the microscope into FIJI and rotating and cropping a rectangular region comprising the S1 from just above layer 1 to the corpus callosum.

The model was trained to classify each cell in the cerebral cortex into one of eight classes based on coexpression of each marker used. The following are the potential cell classes:

(1) $CTIP2^-SATB2^-TBR1^-$ (DAPI only)
(2) $CTIP2^+SATB2^-TBR1^-$
(3) $CTIP2^+SATB2^+TBR1^-$
(4) $CTIP2^+SATB2^+TBR1^+$
(5) $CTIP2^+SATB2^-TBR1^+$
(6) $CTIP2^-SATB2^+TBR1^-$
(7) $CTIP2^-SATB2^+TBR1^+$
(8) $CTIP2^-SATB2^-TBR1^+$

Each image's AI analysis was carefully checked, validating the correct identification of cells and visualizing the overall distribution of labels.

The data resulting from the Biodock AI model is a .csv file containing a comprehensive list of cell measurements obtained from cortical tissue samples. The data included several parameters for each cell: object ID, image origin, class, area, eccentricity, length of major and minor axes, perimeter, solidity, x and y positions and average intensity across four channels.

Further analysis was conducted in the R programming environment. We used key packages including ggplot2 (ref. 84) for data visualization, dplyr[85] for data manipulation and tidyr[86] for data tidying. A critical step in our analysis involved segmenting the cortical area into six equal-sized bins from top to bottom. To achieve this, we calculated the minimum and maximum values of the y position from our data, establishing six equally spaced bins along the y axis. This segmentation allowed us to analyze cell distribution across different cortical layers. Each cell was assigned to one of the six bins based on its y position, facilitating a layer-specific analysis of cell distribution. We then performed a count of cells in each bin, categorizing them into classes based on their expression of markers CTIP2, SATB2 and TBR1.

We computed the percentage of each cell class in each bin relative to the total cell count in that bin. Analyzed data were exported into a new .csv file containing the expanded summary table with cell counts, percentages and other relevant statistics. These data were imported into GraphPad Prism for statistical analyses and graphing. The R script used for this analysis is available at https://doi.org/10.5281/zenodo.10464093 (ref. 87).

EdU quantification and colocalization (P8). EdU quantification and colocalization was performed using Biodock software as described above, training a classifier for classes TBR^+, EdU^- and TBR^+EdU^+.

Fluorescence intensity quantification. Fluorescence intensity quantification was performed in ImageJ/FIJI[88]. The desired region was outlined with the freehand ROI tool. Desired parameters were set by analyze > set measurements and selecting area, integrated density and mean gray value. Analyze > measure was used to acquire the initial intensity value. Three small areas of the image with no fluorescence were selected as background. Analyze > measure was used to acquire background intensity values. Corrected total region fluorescence was calculated as integrated density − (area of selected region × mean fluorescence of background readings).

$GFAP^+$ percent coverage quantification. Images were acquired on an LSM980 microscope at the Boston Children's Hospital Cellular Imaging Core using a ×20 air objective. Quantification was completed in FIJI. Regions of interest (100 × 100 µm) across the S1, corpus callosum or hippocampus were acquired. $GFAP^+$ signal was converted to a binary mask by thresholding, and percent coverage was calculated using analyze > measure with 'area fraction' as set measurement. Three fields of view were acquired from each of three technical replicate images from each P8 CD-1 mouse. Each value reported is an average of these nine images per mouse.

$IBA1^+$ cell quantification. Images were acquired on an LSM980 microscope at the Boston Children's Hospital Cellular Imaging Core using a ×20 air objective. Quantification was completed in FIJI. Regions of interest (100 × 100 µm) across the S1, corpus callosum or hippocampus were acquired. $IBA1^+$ cells were counted manually as cells with staining for $IBA1^+$ and DAPI. Three fields of view were acquired from each of three technical replicate images from each P8 CD-1 mouse. Each value reported is an average of these nine images per mouse.

Oligodendrocyte marker quantification. Images were acquired on an LSM980 microscope at the Boston Children's Hospital Cellular Imaging Core using a ×20 air objective. Quantification was completed in FIJI. Regions of interest (100 × 100 µm) across the corpus callosum were acquired as indicated in Extended Data Fig. 7d. $OLIG2^+$, $CC1^+$ and $SOX2^+$ cells were counted manually. Three to four technical replicate images were acquired from serial brain sections from P8 CD-1 mice. Each value reported is an average of these technical replicates.

PHH3 quantification. PHH3 quantification in the embryonic cortex, MGE and LGE of CD-1 mice was performed in QuPath-0.5.1. Images were acquired on an LSM980 microscope using a ×20 air objective. The resulting .czi files were imported into QuPath for analysis. Annotations were drawn over the appropriate region of interest as indicated in Fig. 4b. The Cell Detection tool was then used to quantify $PHH3^+$ cells per 100 µm of ventricular surface. The following parameters were used in the Cell Detection tool: detection channel AF647-T1, requested pixel size 0.5 µm, background radius 5 µm, use opening by reconstruction, median filter radius 0.5 µm, sigma 3 µm, minimum area 10 μm^2, maximum area 400 μm^2, threshold 300, cell expansion 11.6138 µm, include cell nucleus, smooth boundaries, make measurements.

Immunoblotting

For E16.5 embryos, the time point reported for western blotting and silver stain experiments, we acquired 2–3 µl of CSF per CD-1 mouse embryo. We pooled the same number of litters per biological replicate. Equal volumes of pooled CSF were used for silver staining and western blotting. In total, 0.5 µl of pooled CSF was loaded per well for silver stains and 4 µl of CSF for western blots. We used Ponceau or Coomassie Blue staining to visualize loading. For CSF studies, our practice is to control for volume rather than total protein. As demonstrated in Fig. 1k, overall CSF protein content increases following apocrine secretion. Normalizing by total protein could obscure the very proteins introduced through secretion, undermining the biological insights.

Embryonic CSF was collected and centrifuged (10,000*g* for 5 min), flash-frozen on dry ice and stored at −80°C. Samples were denatured in 2% SDS supplemented with 2-mercaptoethanol by heating at 70 °C for 10 min. Equal amounts of CSF were loaded and separated by electrophoresis in a Bio-Rad 4–15% Mini-PROTEAN TGX Precast protein gel (15-well, 15 µl; Bio-Rad, 4561086; 250 V, 25 min), transferred to a nitrocellulose membrane (Bio-Rad Trans-Blot Turbo Transfer System, 1.0 A, 30 min), blocked for 60 min in filtered 5% milk in TBST (Tris-buffered saline with 0.1% Tween® 20 detergent), incubated with primary antibodies overnight at 4 °C followed by horseradish peroxidase-conjugated secondary antibodies (1:1,000) for 2 h and visualized with ECL or ECL select substrate.

Silver stain. Silver staining was performed on a NuPAGE 4–12% Bis-Tris gel (Invitrogen, NP0322) loaded with 0.5 µl of embryonic CSF per lane. After electrophoresis, silver staining was performed using a Invitrogen SilverQuest Staining kit (Invitrogen, LC6070) according to the manufacturer's instructions.

Immunostaining

ChP explants. ChP explants were dissected from CD-1, C57BL/6J or HTr2cLSL mice and fixed in 4% PFA for 10 min at room temperature[69]. Samples were incubated with primary antibodies overnight at 4 °C with shaking and with secondary antibodies at room temperature for 2 h with shaking. All antibodies were diluted in 0.1% Triton X-100 in PBS. No blocking or antigen retrieval methods were used. All samples were counterstained with Hoechst 33342 (Invitrogen, H3570; 1:10,000) and mounted onto slides using Fluoromount-G (SouthernBiotech).

Brain sections. Postnatal animals were perfused with PBS followed by 4% PFA. The brains were quickly dissected and postfixed with 4% PFA overnight. Samples were cryoprotected and prepared for embedding at 4 °C with 10% sucrose, 20% sucrose, 30% sucrose, a 1:1 mixture of 30% sucrose and OCT (overnight) and OCT (1 h on ice). Samples were then frozen in OCT. Antigen retrieval and blocking were not performed. Cryosections were permeabilized (0.1% Triton X-100 in PBS), incubated with primary antibodies at 4 °C overnight and then with secondary antibodies for 2 h at room temperature. Hoechst 33342 (Invitrogen, H3570; 1:10,000, 5 min at room temperature) was used to visualize nuclei. Sections were mounted on glass slides with Fluoromount-G (SouthernBiotech). Images were acquired using a Zeiss LSM710 or LSM980 confocal microscope with a ×20 objective. ZEN Black software was used for image acquisition, and ZEN Blue software was used for Airy processing.

MIA

For timed pregnancies, CD-1 females were checked for plugs, and the date of the plug was noted as E0.5. Body weight was monitored every 3–4 days, and ultrasound was available to help confirm gestational age. On E12.5, pregnant dams received a single dose (20 mg per kg (body weight), i.p.) of poly(I:C) (Sigma Aldrich) or saline as a vehicle control.

Placenta-attached ex vivo imaging

Timed-pregnant E16.5 female mice were anesthetized with urethane (1.5 g per kg (body weight) i.p. of 10 µl per g (body weight) of 15% urethane in water) and placed on a heating pad. Mice were monitored until unresponsive to toe pinch and palpebral reflexes were present but weak (~30 min). Mice were then given ketamine (0.066 mg per g (body weight) i.p.) to cause deep anesthesia, withdrawal and palpebral reflexes not present (~15 min). Anesthetic depth was checked throughout surgery, and additional doses of 0.066 mg per g (body weight) ketamine were administered as needed.

A laparotomy was performed, and *FoxJ1-cre*::*Ai95D*(RCL-GCaMP6f)-D embryos were gently exposed. Vasculature labeling was achieved by adapting a previous protocol[89], where 3.5 ml of 5 mg ml^{-1} Texas Red Dextran (70 kD; Thermo Fisher Scientific) was delivered into the developing liver using a fine-tip glass capillary tube. Samples were kept moist during the following 5-min circulation time using warm HBSS. The embryo and placenta were then separated from the dam and carefully positioned in our three-dimensional-printed scaffolding such that the back of the head was facing upward. The skin and skull over the 4V were removed to expose the ventricle and 4V ChP. The embryo in the scaffold was then transferred into an imaging chamber filled with continuously circulating aCSF at 37 °C (Alzet formulation as provided online at https://www.alzet.com/guide-to-use/preparation-of-artificial-csf/; 150 mM Na, 3 mM K, 1.4 mM Ca, 0.8 mM Mg, 1 mM P and 155 mM Cl).

Two-photon imaging of epithelial cells was performed using a resonant-scanning two-photon microscope (Olympus MPE-RS Multiphoton Microscope; 12.8 frames per s; 512 × 512 pixels per frame; 0.16 volumes per s, 81 planes per volume; volume size: 254 × 254 × 400 mm^3) and a ×25/1.0-NA objective (Olympus XLPLN25XSVMP2, 4 mm working distance) with 1.3× zoom (394 × 394 mm^2). Volume scanning was achieved by using a piezoelectric microscope stage (nPFocus250). Laser power at 940 nm (Mai Tai DeepSee laser, Spectra Physics) measured below the objective was 30–40 mW.

Methods related to anesthetic use and its impact. Pregnant dams at E16.5 were anesthetized with one of the following agents before drug administration:

- Isoflurane: 1–2% inhalation anesthesia delivered via nose cone.
- Urethane: 1.5 g per kg (body weight) i.p. injection of 15% (wt/vol) urethane solution in sterile water.
- Ketamine/xylazine: combination of ketamine (100 mg per kg (body weight)) and xylazine (10 mg per kg (body weight)) administered intraperitoneally.

WAY-161503 (3 mg per kg (body weight)) or vehicle was administered subcutaneously to anesthetized dams. Thirty minutes after injections, embryos were collected, and ChP tissues were dissected for RT–qPCR analysis of *Fos* expression or fixed for immunostaining.

Protein-retention expansion microscopy

Protein-retention expansion microscopy was performed using established protocols[21] on ChP from CD-1 mice. We used the following reagents: acryloyl-X SE (Thermo Fisher Scientific, A20770); Proteinase K buffered aqueous glycerol solution, for molecular biology, >800 U ml^{-1} (Sigma, P4850-5ML); ammonium persulfate (Sigma, A3678-100G), 4-hydroxy-TEMPO (Sigma, 176141-5G), acrylamide (Sigma, A9099-500G), *N*-*N*′-methylenebisacrylamide (Sigma, 146072-100G), poly-L-lysine solution (0.1%) in water (Millipore Sigma, P8920-100ML) and anhydrous DMSO (Sigma, 276855-100ML). Of note, only sodium acrylate from Combi-Blocks (QC-1489, 98% purity, CAS number 7446-81-3, formula weight 94.0) worked in our hands. Images were acquired with a Zeiss LSM710 confocal microscope with a ×63/1.2-NA water immersion objective.

Proteomics

CSF was collected from E16.5 CD-1 mice. A fine glass capillary was inserted into the cisterna magna to withdraw CSF. Samples containing blood or tissue were discarded. CSF from five litters of embryos was pooled for each sample, as the SomaScan assay used required submission of 100 µl of CSF, and each E16.5 embryo yields ~2–3 µl of CSF. Data reflect three biological replicates (pooled samples) each for a vehicle-injected control condition and a WAY-161503 injection condition. Collected CSF samples were immediately flash-frozen on dry ice and transferred to −80 °C for storage.

Proteomic profiling was performed at the Beth Israel Deaconess Medical Center Genomics, Proteomics, Bioinformatics, and

Systems Biology Center using the oligonucleotide aptamer-based proteomics technology SomaScan[90], provided by SomaLogic (SomaScan Assay v4.1), according to the manufacturer's protocol. SomaScan Assay v4.1 uses 7,322 high-affinity distinct aptamer reagents to measure the expression of 6,596 unique proteins. SomaLogic's proprietary protein-capture reagents called 'SOMAmers' (slow off-rate modified aptamer) leverage Cy3-labeled, chemically modified, short single-stranded DNA sequences known as aptamers that form three-dimensional structures like antibodies and based on their unique nucleotide sequences can bind with high affinity and selectivity to distinct proteins. The readouts for the assay are custom microarray chips containing complementary oligonucleotides to each fluorescently labeled SOMAmer. Three provided kit controls and one no-protein buffer control were analyzed in parallel with the CSF samples to adjust for intrarun variation. Median normalization and calibration of the SomaScan data were performed according to standard quality control protocols at SomaLogic. The final assay readout is in relative fluorescence units, an arbitrary unit directly proportional to protein expression.

Proteomics analysis: R

Data acquisition and preprocessing. The normalized dataset for this study was obtained from SomaLogic and stored in .adat format. The file, named 'original.adat', was processed using a script written in R (version 4.1.2). The readat package was used to import the raw data. Sample classification was performed based on the experimental design, with samples grouped as saline, WAY-161503 or quality control

Data analysis and visualization. R packages, including reshape2, magrittr, dplyr, ggplot2, limma, Biobase, countdata, ggrepel, topGO, org.Hs.eg.db, glue, tibble, Rgraphviz, enrichplot, DOSE and ggvenn, were used for data analysis and visualization[84,85,91–103]. The limma package was used for linear regression and analysis, and the countdata package facilitated fold change analysis.

Proteins of interest were identified based on the largest between-group variation, and their intensity levels were visualized using ggplot2. Differential expression analysis was performed, and results were visualized as volcano plots. Gene names were standardized using the org.Hs.eg.db package, which provides genome-wide annotation for human genes.

Gene Ontology enrichment analysis. The topGO package performed Gene Ontology (GO) enrichment analysis. This analysis focused on identifying enriched GO terms within the list of differentially expressed genes by using Fisher's exact test and the Kolmogorov–Smirnov test. The GO terms were categorized into three main ontologies: biological process, molecular function and cellular component.

Statistical analysis. Statistical significance for differential expression was determined using a combination of fold change and *t*-test *P* values. For GO enrichment analysis, significance was assessed using Fisher's exact and Kolmogorov–Smirnov tests, as implemented in the topGO package. Adjusted *P* values were calculated to control for multiple testing.

Data visualization. Data visualization was performed using ggplot2, Rgraphviz, enrichplot and ggvenn. This included the generation of volcano plots for differential expression analysis, heat maps for visualizing gene expression patterns and Venn diagrams to illustrate the overlap between different protein sets. Gene Ontology terms were visualized using ggplot2 and ggpubr, focusing on terms with a significant number of genes and highlighting the statistical significance using a star-based system.

The R script used for this analysis is available at https://doi.org/10.5281/zenodo.10464124 (ref. 104).

Proteomics analysis: IPA

IPA software (Qiagen) was used[105].

Importing data. Once differentially abundant proteins were identified in R, a list of up- and downregulated proteins and their expression values was used for IPA. The data file included Entrez Gene Symbol identifiers for each protein along with their corresponding fold change values.

Core analysis. IPA core analysis included the identification of enriched pathways, upstream regulators, molecular networks and biological functions.

Pathway and network identification. IPA identified relevant pathways enriched in the dataset. Molecular interaction networks were generated, highlighting key proteins and their interactions within the context of the identified pathways.

Upstream regulator analysis. IPA upstream regulator analysis was used to predict potential upstream molecules that could be responsible for the observed changes in protein expression. IPA provided statistical scores for enrichment of pathways and networks based on the input data. The significance of the association between the dataset and canonical pathways was measured in terms of *P* values, calculated using Fisher's exact test.

Data interpretation and visualization. IPA offered various tools for the interpretation and visualization of results. This included graphical representations of pathways, networks and their components, with options to customize views for detailed analysis. The results were interpreted in the context of current biological knowledge and relevant literature integrated within IPA's database. The analysis was performed on a standard computing setup with internet access to use the web-based IPA software.

Quantification and statistical analysis

To achieve robust and unbiased results, we performed our analyses across multiple samples, prospectively randomized treatment group via random number generation, quantified results depending on genotype in a double-blinded manner and performed rigorous pre and post hoc statistical analyses to test our hypotheses. We consulted with Harvard statisticians (Boston Children's Hospital, Beth Israel Deaconess Medical Center and Broad Institute) to ensure proper calculations of power analyses and statistical methods, including accounting for multiple comparisons and covariates. We performed an equal number of experiments on male and female mice (except for pregnant mice, which were all female) and carefully examined sex as a biological variable in our analyses. For each experiment, pilot studies were used to determine variance, and two-tailed power analyses determined optimal group size for $\alpha = 0.05$ and $\beta = 0.80$. Biological replicates (N) were defined as samples from individual animals, analyzed either in the same experiment or within multiple experiments, except when individual animals could not provide sufficient sample material (that is, CSF), which required pooling samples from multiple animals into one biological replicate, as described earlier.

Statistical analyses were performed using Prism (GraphPad, v9) or R (version 4.1.2). Outliers were excluded using the ROUT method ($Q = 1\%$). Data distribution was assessed using the Shapiro–Wilk normality test, and homogeneity of variances between datasets was evaluated using *F*-tests or Bartlett's tests. Parametric tests were used when data were normally distributed, and variances were approximately equal; otherwise, nonparametric alternatives were applied.

Specific statistical tests were selected based on the data and analysis goals. Student's two-tailed unpaired *t*-tests were used for comparisons with one independent variable and two groups, provided that data followed a normal distribution and variances were equal.

If variances were unequal, a Welch's two-tailed unpaired *t*-test was applied. A one-way ANOVA with a Tukey post hoc correction was used for analyses with one independent variable and more than two groups, provided that data followed a normal distribution. A two-way ANOVA with a Sidak post hoc correction was used when two independent variables were tested. Nonparametric alternatives were used for data that did not follow a normal distribution, specifically, a Mann–Whitney *U*-test for comparisons of two groups and a Kruskal–Wallis test with Dunn's multiple comparisons correction for more than two groups. For cell density and regional quantifications, tests were selected based on the relevance of interactions between variables. In cases where exploring interactions was not relevant, multiple *t*-tests or one-way ANOVAs were used.

Data are presented as mean ± s.d. If multiple measurements were taken from a single individual, data are presented as mean ± s.e.m. Please refer to the figure legends for sample sizes. *P* values of <0.05 were considered significant. Exact *P* values are marked in the figures where space allows.

RT–qPCR

ChP tissues were rapidly microdissected from CD-1, C57BL/6J or HTr-2cLSL mice, immediately frozen on dry ice and stored at −80 °C. A Monarch Total RNA Miniprep kit (New England Biolabs, T2010S) was used for total RNA isolation, eluting in 50 µl of nuclease-free water. Each biological replicate consisted of a pair of LV ChP explants or one 4V explant. The extracted RNA was quantified using a spectrophotometer, and 100 ng of RNA was reverse transcribed into cDNA using a LunaScript RT Master Mix kit (New England Biolabs, E3025L). qPCR reactions used specific primers and were performed in triplicate with Applied Biosystems TaqMan Gene Expression Master Mix (Thermo Fisher Scientific, 4369016). The probes used included Mm00487425_m1 (*Fos*, FAM-MGB; Thermo Fisher Scientific, 4331182), Mm00434127_m1 (*Htr2c*, FAM-MGB; Thermo Fisher Scientific, 4331182), Mm00441712_s1 (*Sry*, FAM-MGB; Thermo Fisher Scientific, 4331182) and Hs99999901_s1 (eukaryotic 18S rRNA, VIC-MGB; Thermo Fisher Scientific, 4331182). The cycling process was performed using a Roche LightCycler 480II. The following PCR cycling conditions were used: initial denaturation at 95 °C for 10 min, followed by 40 cycles of 95 °C for 15 s and 60 °C for 1 min. All reactions were performed in triplicate. Relative gene expression analysis was conducted using the change in cycling threshold ($2^{-\Delta\Delta C_t}$) method[106], normalizing expression levels to 18S rRNA as the internal control.

RNAScope in situ hybridization

RNAScope in situ hybridization was performed using an RNAScope Multiplex Fluorescent Reagent kit v2 (Advanced Cell Diagnostics, 323100). P30 brains from C57BL/6J or HTr2cLSL mice were perfusion-fixed and subsequently drop-fixed in 4% PFA, after which 14-µm sections were mounted on Superfrost Plus slides and dried at −20 °C for 30 min before processing. For pretreatment, the sections were rehydrated in PBS, followed by graded ethanol dehydration (50%, 70%, 100% and 100%) at room temperature for 5 min each. After air drying, sections were treated with Protease IV (Advanced Cell Diagnostics, 322340) for 30 min at room temperature to ensure optimal probe penetration. Hybridization of the RNAScope probes, including Mm-Htr2c (ACD, 316641) and the negative-control probe DapB (Advanced Cell Diagnostics, 310043), was conducted at 40 °C for 2 h in a HybEZ oven (Advanced Cell Diagnostics). Signal amplification was achieved through a series of sequential amplification steps using AMP 1-FL, AMP 2-FL and AMP 3-FL reagents, each applied for 30 min at 40 °C, with washes in RNAScope Wash Buffer between each step. Fluorescence detection was performed using TSA Plus fluorophores (Akoya Biosciences), diluted 1:1,500 in TSA buffer. For the Htr2c probe, TSA Plus Cyanine 3 was applied for 30 min at room temperature. Images were captured using a Zeiss LSM710 confocal microscope equipped with a ×20 objective.

SEM

LV ChP tissue from adult and embryonic CD-1, C57BL/6J or HTr2cLSL mice was microdissected and postfixed in 1.0% osmium tetroxide in 0.1 M cacodylate buffer (pH 7.4) for 1 h at room temperature. Following postfixation, the samples were rinsed with buffer and dehydrated through a graded series of ethanol. The specimens were then critical point dried with CO_2 using a Samdri PVT-3 critical point dryer (Tousimis). The specimens were attached to specimen mounts using conductive adhesive tabs, coated with 5-nm platinum using a Cressington 208HR sputter coater (Cressington Scientific Instruments). Imaging was conducted on a Hitachi S-4700 FESEM. Electron microscopy imaging, consultation and services were performed in the HMS Electron Microscopy Facility and the NEU Electron Microscopy Facility.

Transmission electron microscopy

LV ChP from CD-1 mice was microdissected in HBSS (Thermo Fisher Scientific) and drop-fixed immediately in FGP (5% glutaraldehyde, 2.5% PFA and 0.06% picric acid in 0.2 M sodium cacodylate buffer, pH 7.4). After 2 h at room temperature, the tissue was washed in 0.1 M cacodylate buffer and postfixed with 1% osmium tetroxide/1.5% potassium ferrocyanide for 1 h, washed twice in water, washed once in 50 mM maleate buffer (MB; pH 5.15), incubated in 1% uranyl acetate in MB for 1 h, washed once in MB, washed twice in water and dehydrated in a series of increasingly concentrated alcohol (10 min each; 50%, 70%, 90% and 2 × 10 min 100%). The samples were immersed in propylene oxide for 1 h and infiltrated overnight in a 1:1 mixture of propylene oxide and TAAB Epon (TAAB Laboratories Equipment). The following day, the samples were embedded in TAAB Epon and polymerized at 60 °C for 48 h. Ultrathin sections (about 80 nm) were cut on a Reichert Ultracut-S microtome and placed on copper grids stained with lead citrate. Images were acquired with a JEOL 1200EX transmission electron microscope and recorded with an AMT 2k CCD camera (Electron Microscopy Facility, Harvard Medical School).

Reporting summary

Further information on research design is available in the Nature Portfolio Reporting Summary linked to this article.

Data availability

We have made our SomaScan proteomics data publicly accessible through Zenodo at https://zenodo.org/records/10465931 (ref. 107). Previously published single-cell RNA-sequencing data used in the analyses can be accessed via GSE168704. Additional data that support the findings of this study are available from the corresponding author upon request. Source data are provided with this paper.

Code availability

R scripts used for analysis are available through Zenodo. The cortical layer cell counting script can be accessed at https://zenodo.org/records/10464093 (ref. 87). SomaScan proteomics analysis script at https://zenodo.org/records/10464124 (ref. 104).

References

70. McFarlane, H. G. et al. Autism-like behavioral phenotypes in BTBR T^{tf}/J mice. *Genes Brain Behav.* **7**, 152–163 (2008).
71. Silverman, J. L. et al. Negative allosteric modulation of the mGluR5 receptor reduces repetitive behaviors and rescues social deficits in mouse models of autism. *Sci. Transl. Med.* **4**, 131ra51 (2012).
72. Silverman, J. L. et al. Sociability and motor functions in *Shank1* mutant mice. *Brain Res.* **1380**, 120–137 (2011).
73. Whitney, G., Coble, J. R., Stockton, M. D. & Tilson, E. F. Ultrasonic emissions: do they facilitate courtship of mice. *J. Comp. Physiol. Psychol.* **84**, 445–452 (1973).
74. Maggio, J. C. & Whitney, G. Ultrasonic vocalizing by adult female mice (*Mus musculus*). *J. Comp. Psychol.* **99**, 420–436 (1985).

75. Pietropaolo, S., Guilleminot, A., Martin, B., D'Amato, F. R. & Crusio, W. E. Genetic-background modulation of core and variable autistic-like symptoms in *Fmr1* knock-out mice. *PLoS ONE* **6**, e17073 (2011).
76. Oddi, D. et al. Early social enrichment rescues adult behavioral and brain abnormalities in a mouse model of fragile X syndrome. *Neuropsychopharmacology* **40**, 1113–1122 (2015).
77. Gauducheau, M. et al. Age-specific autistic-like behaviors in heterozygous *Fmr1*-KO female mice. *Autism Res.* **10**, 1067–1078 (2017).
78. Scattoni, M. L., Ricceri, L. & Crawley, J. N. Unusual repertoire of vocalizations in adult BTBR T^{+tf}/J mice during three types of social encounters. *Genes Brain Behav.* **10**, 44–56 (2011).
79. Caruso, A., Ricceri, L. & Scattoni, M. L. Ultrasonic vocalizations as a fundamental tool for early and adult behavioral phenotyping of autism spectrum disorder rodent models. *Neurosci. Biobehav. Rev.* **116**, 31–43 (2020).
80. Premoli, M. et al. Specific profile of ultrasonic communication in a mouse model of neurodevelopmental disorders. *Sci. Rep.* **9**, 15912 (2019).
81. Xu, H. et al. Choroid plexus NKCC1 mediates cerebrospinal fluid clearance during mouse early postnatal development. *Nat. Commun.* **12**, 447 (2021).
82. Bankhead, P. et al. QuPath: open source software for digital pathology image analysis. *Sci. Rep.* **7**, 16878 (2017).
83. Biodock AI software platform (Biodock Inc., 2023).
84. Wickham, H. *ggplot2: Elegant Graphics for Data Analysis* (Springer, 2016).
85. Wickham, H., Francois, R., Henry, L., Muller, K. & Vaughan, D. dplyr: a grammar of data manipulation. R package version 1.1.4 https://github.com/tidyverse/dplyr (2023).
86. Wickham, H., Vaughan, D. & Girlich, M. tidyr: tidy messy data. R version 2.0.3.9000 https://tidyr.tidyverse.org/ (2023).
87. Courtney, Y. Cortical layer cell counting. *Zenodo* https://doi.org/10.5281/zenodo.10464093 (2024).
88. Schindelin, J. et al. Fiji: an open-source platform for biological-image analysis. *Nat. Methods* **9**, 676–682 (2012).
89. Ben-Zvi, A. et al. MFSD2A is critical for the formation and function of the blood–brain barrier. *Nature* **509**, 507–511 (2014).
90. SomaScan Assay v. 4.1 (SomaLogic, 2022).
91. Wickham, H. Reshaping data with the reshape package. *J. Stat. Softw.* **21**, 1–20 (2007).
92. Bache, S. M. & Wickham, H. magrittr: a forward-pipe operator for R. R version 2.0.3.9000 https://github.com/tidyverse/magrittr (2022).
93. Ritchie, M. E. et al. limma powers differential expression analyses for RNA-sequencing and microarray studies. *Nucleic Acids Res.* **43**, e47 (2015).
94. Huber, W. et al. Orchestrating high-throughput genomic analysis with Bioconductor. *Nat. Methods* **12**, 115–121 (2015).
95. Pham, T. V., Piersma, S. R., Warmoes, M. & Jimenez, C. R. On the β-binomial model for analysis of spectral count data in label-free tandem mass spectrometry-based proteomics. *Bioinformatics* **26**, 363–369 (2010).
96. Slowikowski, K. ggrepel: automatically position non-overlapping text labels with 'ggplot2'. R version 0.9.6 https://cran.r-project.org/web/packages/ggrepel/index.html (2024)
97. Alexa, A. & Rahnenfuhrer, J. topGO: enrichment analysis for Gene Ontology. *Bioconductor* https://doi.org/10.18129/B9.bioc.topGO (2023).
98. Carlson, M. org.Hs.eg.db: genome wide annotation for human. *Bioconductor* https://doi.org/10.18129/B9.bioc.org.Hs.eg.db (2019).
99. Hester, J. & Bryan, J. glue: interpreted string literals. R version 1.8.0 https://cloud.r-project.org/web/packages/glue/index.html (2022).
100. Muller, K. & Wickham, H. tibble: simple data frames. R version 3.2.1 https://github.com/tidyverse/tibble (2023).
101. Yu, G. enrichplot. *Bioconductor* https://doi.org/10.18129/B9.BIOC.ENRICHPLOT (2018).
102. Yan, L. ggvenn: draw Venn diagram by 'ggplot2'. https://cran.r-project.org/package=ggvenn (2023).
103. Kassambara, A. ggpubr: 'ggplot2' based publication ready plots. R version 0.6.0 https://cran.r-project.org/web/packages/ggpubr/index (2023).
104. Courtney, Y. Choroid plexus apocrine secretion CSF SomaScan ADAT processing and analysis. *Zenodo* https://doi.org/10.5281/zenodo.10464124 (2024).
105. Krämer, A., Green, J., Pollard, J. & Tugendreich, S. Causal analysis approaches in Ingenuity Pathway Analysis. *Bioinformatics* **30**, 523–530 (2014).
106. Livak, K. J. & Schmittgen, T. D. Analysis of relative gene expression data using real-time quantitative PCR and the $2^{-\Delta\Delta C_t}$ method. *Methods* **25**, 402–408 (2001).
107. Courtney, Y. E16.5 Mouse CSF baseline vs. WAY161503 SomaScan ADAT. *Zenodo* https://doi.org/10.5281/zenodo.10465931 (2024).

Acknowledgements

We thank J. Elmquist for sharing *Htr2c-lox*-STOP-*lox* mice. We thank C. Chen, H. Umemori, C.-H. Chien, H. Cramer and the BCH Intellectual and Developmental Disabilities Research Center (IDDRC) Cellular Imaging Core for imaging assistance. We thank M. Andermann, M. Ericsson, A. Nordstrom, the Harvard Medical School Electron Microscopy Facility and the NEU Electron Microscopy Facility for help with sample preparation and imaging. We thank N. Hodgson and the BCH Animal Behavior and Physiology Core for assistance with behavioral tasks and analysis. We thank S. Dillon and the Beth Israel Deaconess Medical Center Genomics, Proteomics, Bioinformatics and Systems Biology Center for help with SomaScan. We thank members of the laboratory of M.K.L., J. Macklis, P. Kaeser, T. Hla and N. Chamberlin for their discussion and comments on the manuscript and E. Yimer (Harvard Summer Honors Undergraduate Research Program and Harvard Griffin Graduate School of Arts and Sciences Research Scholar Initiative) and T. Lacey (Gates Millenium Scholarship) for technical assistance. We acknowledge BioRender.com for assistance with creating several schematics. This work was supported in part by a grant to Harvard University from the Howard Hughes Medical Institute through the James H. Gilliam Fellowships for Advanced Study Program (Y.C.), the National Science Foundation Graduate Research Fellowship (Y.C. and F.B.S.), the William Randolph Hearst Fellowship (N.D.), the Office of Faculty Development/Basic/Translational Research Executive Committee/Clinical and Translational Research Executive Committee Faculty Development Fellowship Award (N.D.), NIH NHLBI R35HL145242 (M.J.H.), NIH P30CA006516 (T.A.L.), Simons Foundation Autism Research Initiative award 610670, Harvard Brain Science Initiative Bipolar Disorder Seed Grant, Human Frontier Science Program research program grant (RGP0063/2018), Kirby Innovation Award, Tommy Fuss Center, New York Stem Cell Foundation, NIH R01NS088566, R01NS129823 and RF1DA048790 (M.K.L.) and Boston Children's Hospital Intellectual and Developmental Disabilities Research Center 1U54HD090255, NIH P50HD105351 and S10OD016453 to the IDDRC Cellular Imaging Core. This content is solely the responsibility of the authors and does not necessarily represent the official views of the NIH.

Author contributions

Conceived and designed the study: Y.C., N.D. and M.K.L. Performed experiments and collected data: Y.C., J.P.H., N.D., F.B.S., O.V.C. and C.S. Data curation and analysis: Y.C., J.P.H., N.D., F.B.S., C.S. and T.A.L. Provided resources: Y.Z. and M.J.H. Supervision and funding: M.K.L. Writing, original draft: Y.C. and M.K.L. Writing, review and editing: all authors.

Competing Interests
The authors declare that they have no competing interests.

Additional information
Extended data is available for this paper at https://doi.org/10.1038/s41593-025-01972-9.

Supplementary information The online version contains supplementary material available at https://doi.org/10.1038/s41593-025-01972-9.

Correspondence and requests for materials should be addressed to Maria K. Lehtinen.

Peer review information *Nature Neuroscience* thanks Stewart Anderson, Nicoletta Kessaris and the other, anonymous, reviewer(s) for their contribution to the peer review of this work.

https://doi.org/10.1038/s41593-025-01972-9

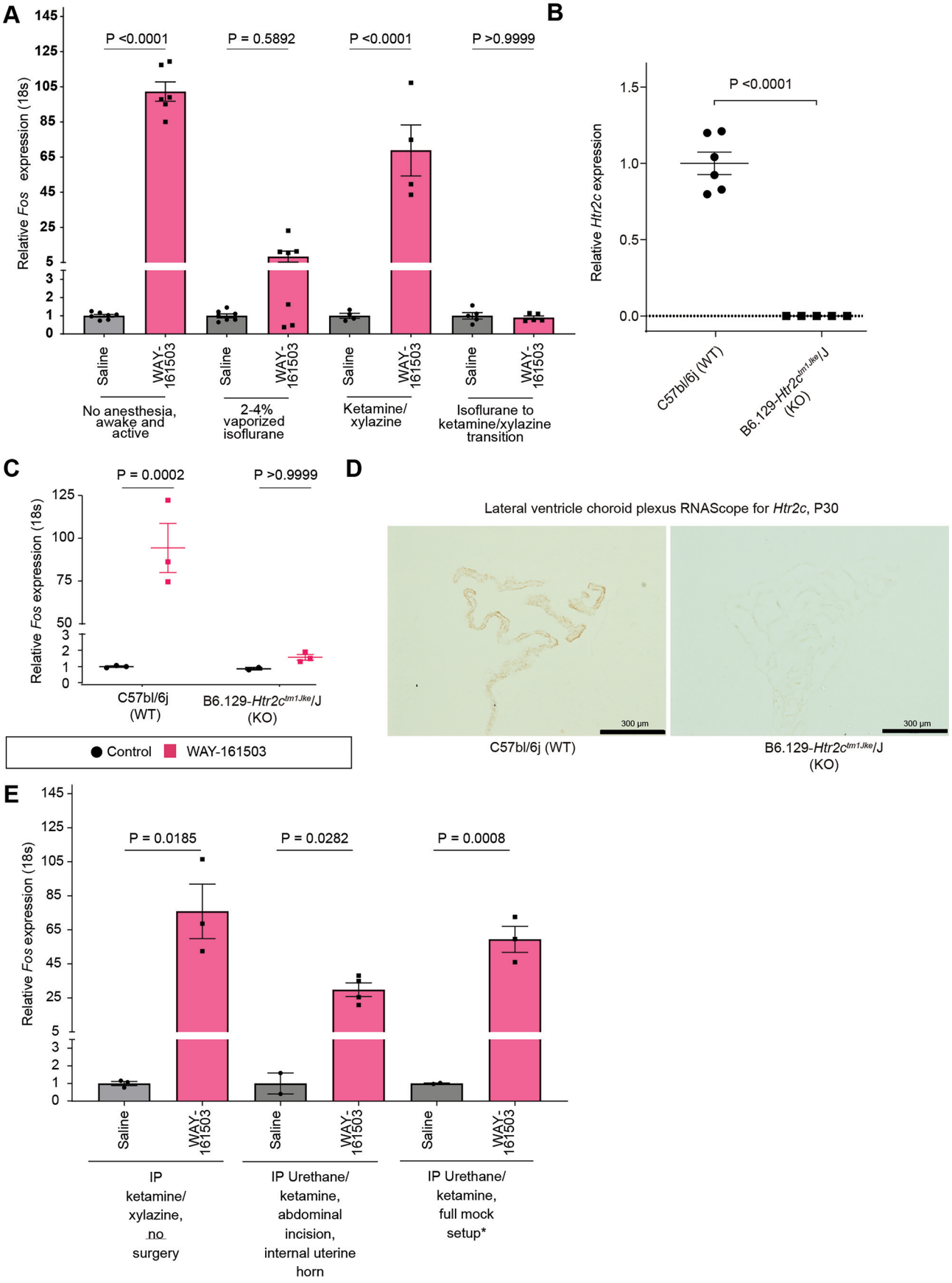

Extended Data Fig. 1 | See next page for caption.

https://doi.org/10.1038/s41593-025-01972-9

Extended Data Fig. 1 | Maternal anesthesia method impacts maternal-fetal transmission of WAY-161503 and ChP activation. (**A**) Isofluorane inhibits E16.5 *Fos* induction. No anesthesia control n = 7, WAY n = 6. 2-4% vaporized isofluorane control n = 7, WAY n = 7. Ketamine/xylazine control n = 4, WAY n = 4. Isofluorane to ketamine/xylazine transition control n = 5, WAY n = 5. (**B**) qPCR validation of *Htr2c* knockout mouse lines. N = 7 wild-type and 5 KO embryos. (**C**) WAY-161503 does not induce activity-dependent gene expression in ChP from *Htr2c* knockout mouse line, n = 3 embryos/condition. (**D**) Representative images of RNAscope validation of *Htr2c* knockout in LV ChP. Scale bars 200 µm. (**E**) Urethane maintains WAY-161503-induced *Fos*. IP ketamine/xylazine, no surgery control n = 3, WAY n = 3. IP urethane/ketamine, abdominal incision, internal uterine horn control n = 3, WAY n = 4. IP urethane/ketamine, full mock setup control n = 3, WAY n = 2. Data Presentation: All data presented as mean ± SEM. P values from two-way ANOVA with Sidak correction for (**A**), (**C**), and (**E**) and from two-tailed unpaired t-test for (**B**).

https://doi.org/10.1038/s41593-025-01972-9

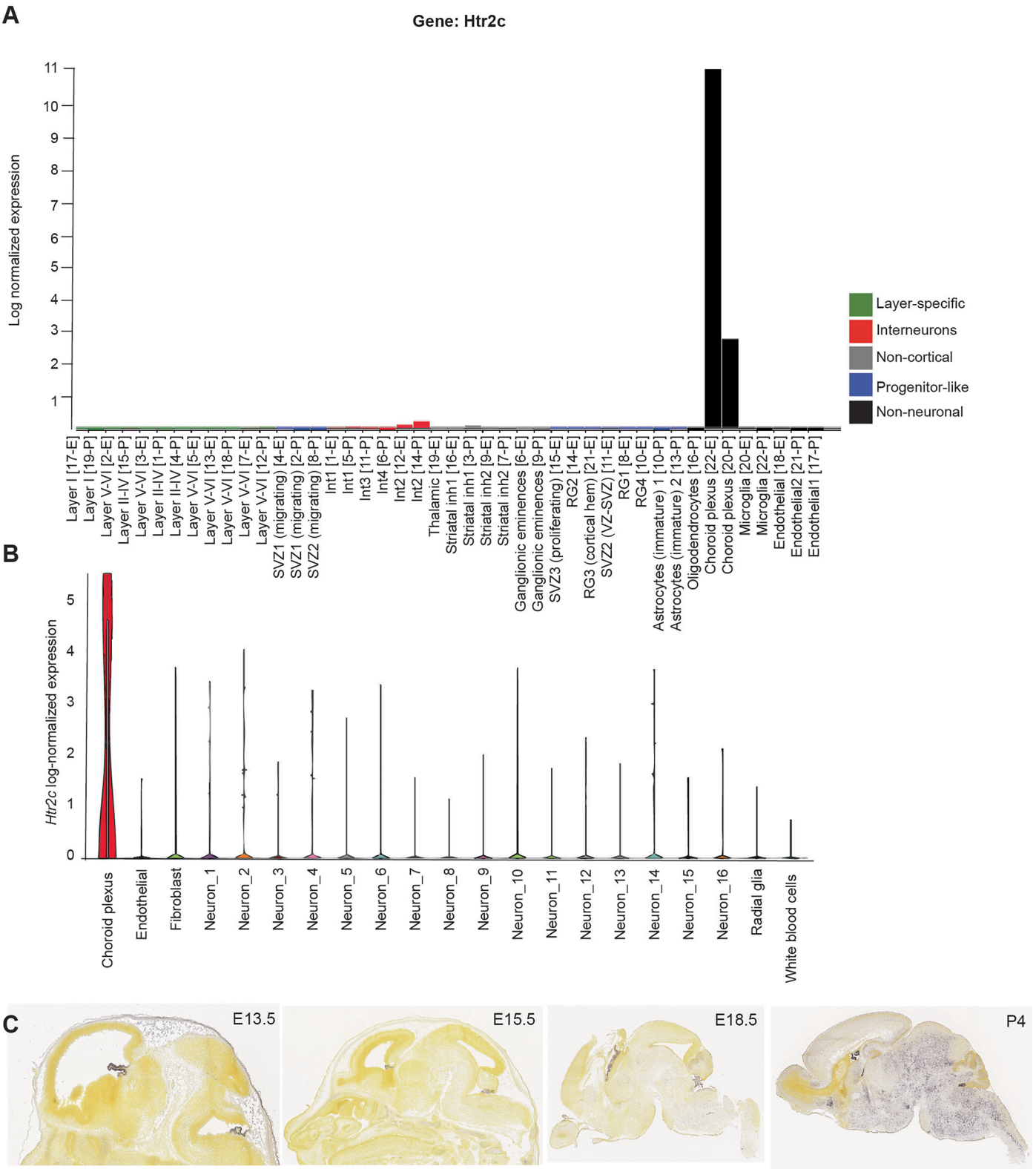

Extended Data Fig. 2 | In the embryonic mouse brain, *Htr2c* is selectively expressed in ChP. (**A**) Bar graph of E14.5 and P0 *Htr2c* expression reveals that, throughout the mouse neocortex, ChP expresses *Htr2c* during embryonic development. Notably, *Htr2c* is not expressed in progenitors. Created with the Zylka Lab's Single-cell transcriptomic analysis of mouse neocortical development gene-by-gene search webpage with data from Loo et al.[1]. https://zylkalab.org/datamousecortex (**B**) Violin plot of E14 *Htr2c* expression demonstrates high ChP *Htr2c* expression in mouse brain at E14.5. created with Broad Institute Single Cell Portal from Mouse E14 brain single nucleus RNA sequencing data gathered for Russell et al.[2]. https://singlecell.broadinstitute.org/single_cell/study/SCP2170/slide-tags-snrna-seq-on-mouse-embryonic-e14-brain (**C**) Expression of *Htr2c* in E13.5, E15.5, E18.5, and P4 mouse brain shows that before E18.5, *Htr2c* is highly and predominantly expressed in ChP. At E18.5, low expression arises in brainstem nuclei. At P4, *Htr2c* expression is widespread. Allen Developing Mouse Brain Atlas, developingmouse.brain-map.org/experiment/show/100047619.

https://doi.org/10.1038/s41593-025-01972-9

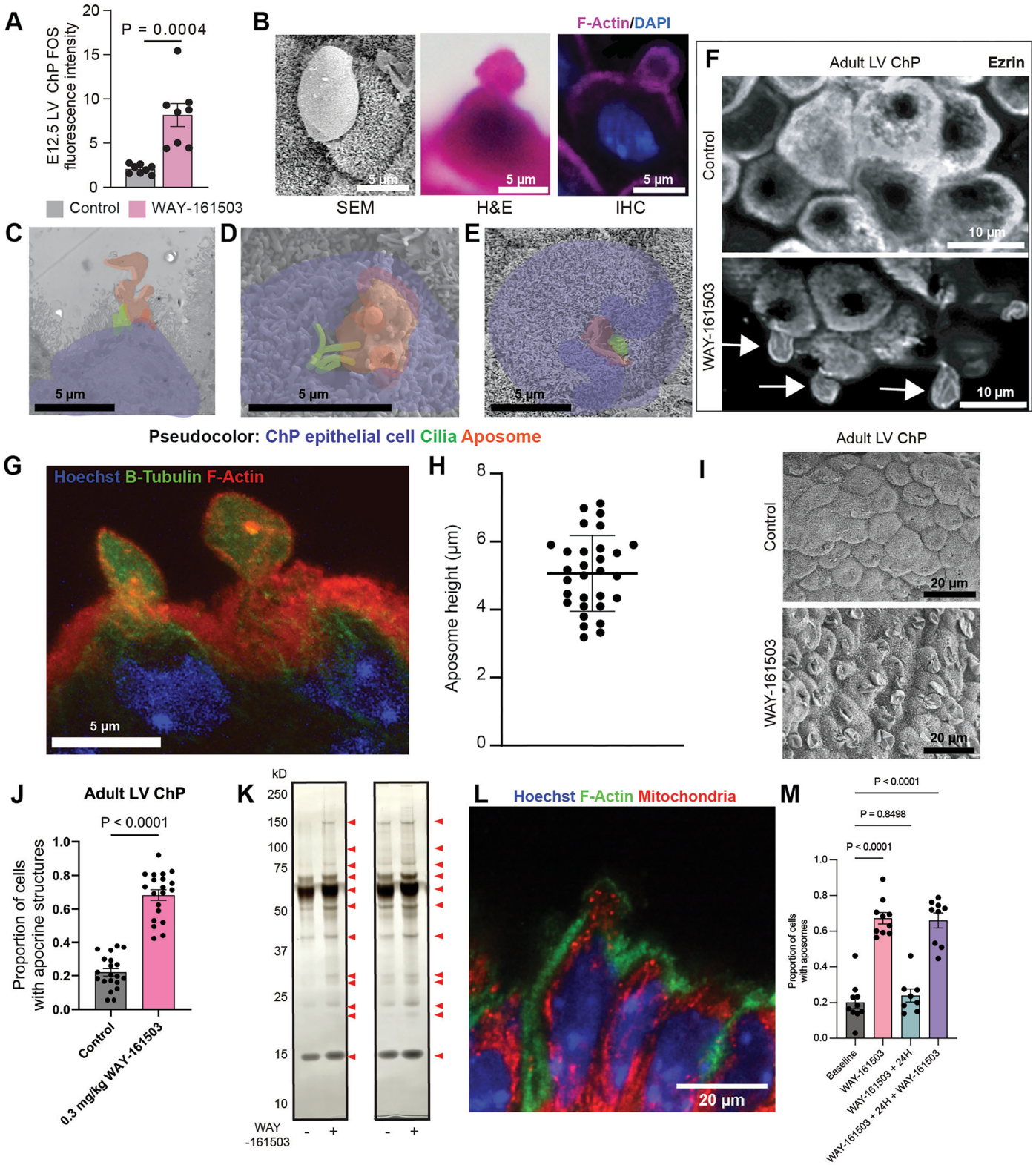

Extended Data Fig. 3 | See next page for caption.

https://doi.org/10.1038/s41593-025-01972-9

Extended Data Fig. 3 | Choroid plexus aposomes. (**A**) Intensity of FOS immunofluorescence in E12.5 ChP, N = 8 embryos from 4 litters/condition. (**B**) Apocrine structures visualized by, from left to right, SEM, H&E stain, and IHC. (**C**) TEM image depicting an E16.5 ChP epithelial cell with an aposome protruding immediately adjacent to cilia. (**D**) SEM image depicting an E16.5 ChP epithelial cell with a collapsed, likely post-secretion aposome protruding immediately adjacent to cilia. (**E**) SEM image depicting an E16.5 epithelial cell with an emerging aposome protruding immediately adjacent to cilia. (**F**) Representative confocal images of control (top) and apocrine (bottom) LV ChP showing the apical depressions, unstained by Ezrin, from which aposomes arise. (**G**) Expansion microscopy image depicting two E16.5 ChP epithelial cells, each with aposomes supported by a network of microtubules. (**H**) Quantification of size of aposomes at E16.5, N = 30 mice from 6 litters. (**I**) SEM of adult LV ChP after control (saline) or WAY-161503 injection. Aposomes quantified in (**J**). (**K**) Two representative silver stains of E16.5 CSF 30 min following maternal saline (control, left) or WAY-161503 (right). Red arrows indicate proteins whose concentration appeared visually to differ between conditions. (**L**) Expansion microscopy image depicting ChP LV epithelial cells, one with an aposome containing mitochondria (Citrate Synthase antibody). (**M**) Quantification of LV ChP aposomes at baseline, 30 min after WAY-161503 injection, 24 h after WAY-161503 injection, or after 2 injections of WAY-161503 at a 24 h interval. Data Presentation: All data presented as mean ± SEM. Scale bars 5 μm unless otherwise noted. P values from two-tailed t-test for (**A**) and (**J**), and from one-way ANOVA with Tukey correction for (**M**).

https://doi.org/10.1038/s41593-025-01972-9

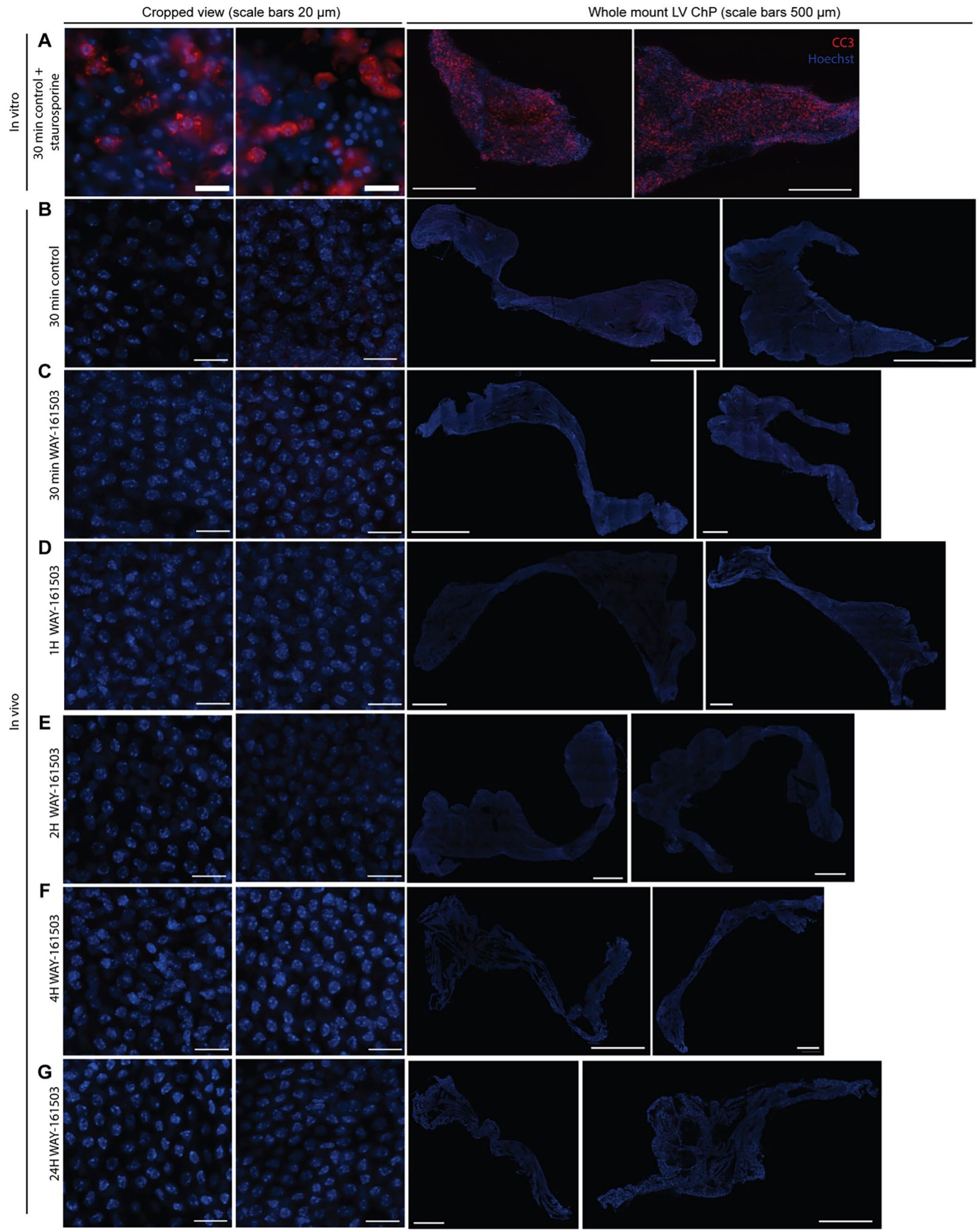

Extended Data Fig. 4 | Choroid plexus apocrine secretion is not apoptotic. Representative confocal images of LV ChP explants, CC3 staining reveals apoptosis in an *in vitro* staurosporine-treated positive control for cell death (**A**), but not following an *in vivo* control injection (**B**) or at various time points after evoking *in vivo* apocrine secretion (**B**)-(**G**). Cropped views on the left, scale bars 20 µm. Whole mount LV ChP views on the right, scale bars 500 µm.

https://doi.org/10.1038/s41593-025-01972-9

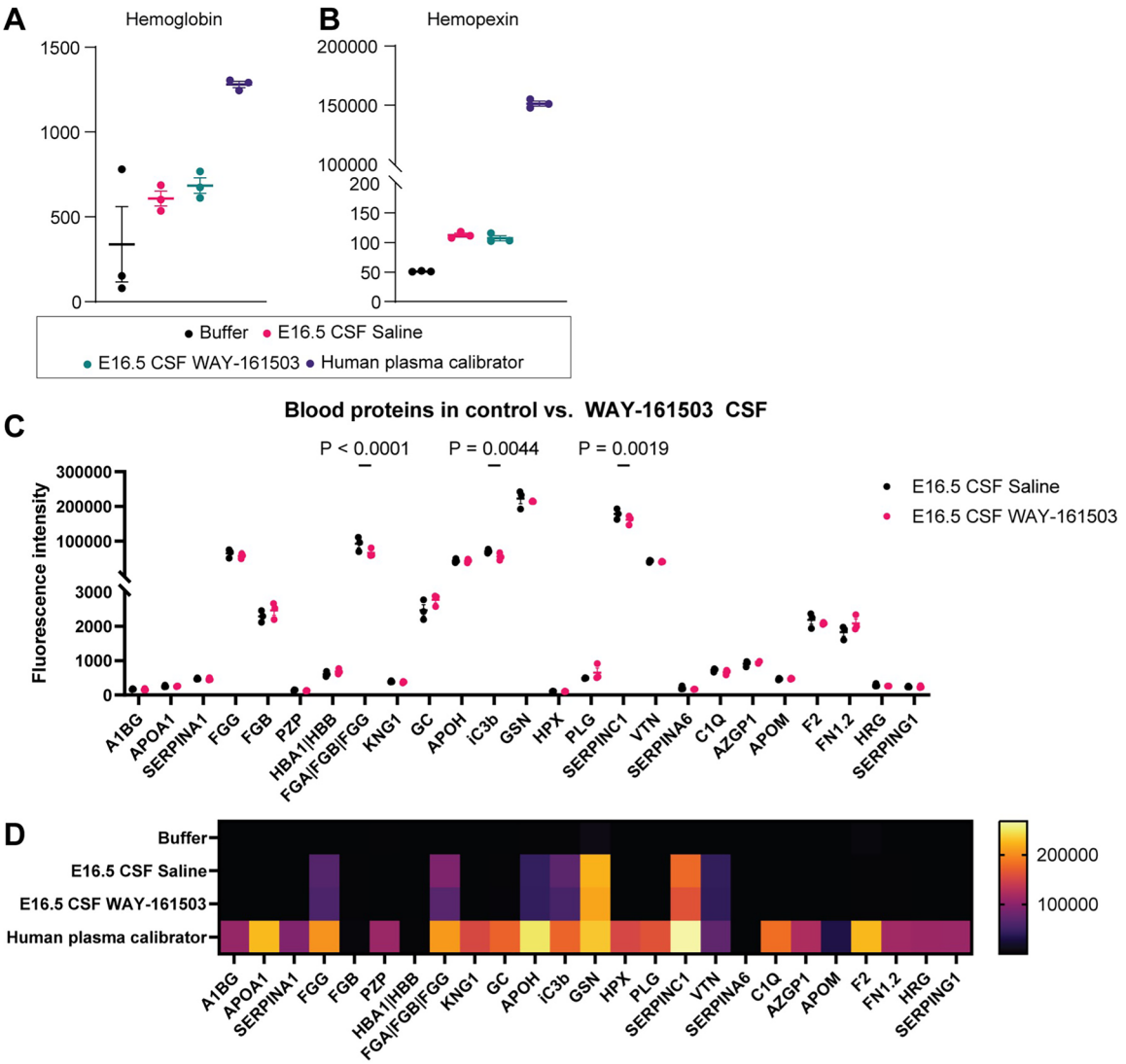

Extended Data Fig. 5 | Blood-derived proteins in embryonic CSF following ChP 5HT2C activation. (**A**) Fluorescence intensity readings for hemoglobin and (**B**) hemopexin levels in E16.5 CSF after maternal saline or WAY-161503 injection, in SomaScan buffer solution, and in SomaScan human plasma calibrator. (**C**) Fluorescence intensity of top 25 common blood-derived proteins in CSF reveals no increases in WAY-161503-treated CSF compared to controls (saline-treated). (**D**) Heatmap summarizing fluorescence intensity of blood-derived proteins detected in CSF across conditions. Data Presentation: All data presented as mean ± SEM. P values from one-way ANOVA with Tukey correction for (**A**) and (**B**), and from two-way ANOVA with Sidak correction for (**C**) and (**D**).

https://doi.org/10.1038/s41593-025-01972-9

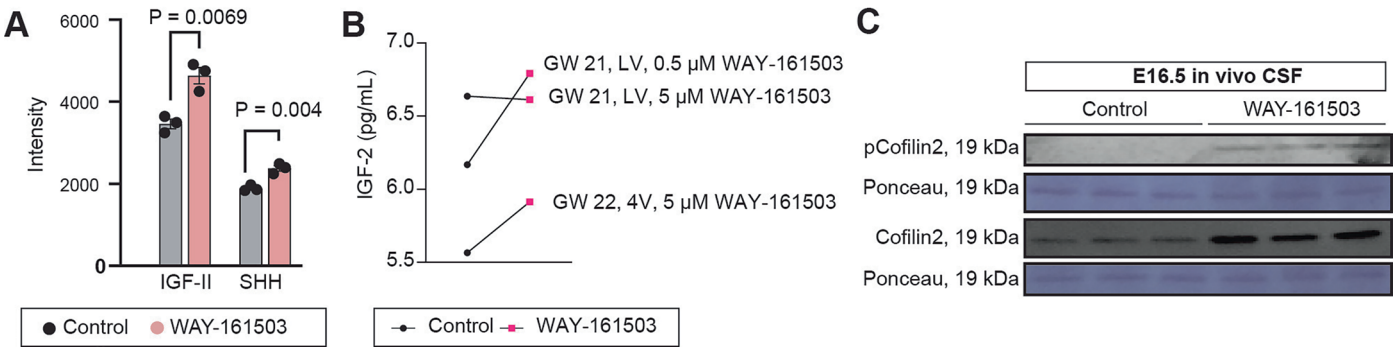

Extended Data Fig. 6 | ChP apocrine proteomics. (**A**) SomaScan intensity measurements for IGF-2 and SHH protein in CSF demonstrate ChP release. N = 3 E16.5 CSF samples, each pooled from 3 litters. (**B**) IGF-2 levels in conditioned aCSF measured by ELISA for each of three human fetal ChP samples. Half of each sample was incubated with vehicle control in aCSF, half with WAY-161503. N = 3. (**C**) Western blot for Cofilin-2 and phospho-Cofilin-2 in CSF from E16.5 embryos 30 min after maternal WAY-161503 delivery. Cropped Ponceau stain of each membrane displayed as loading control, full blots and Ponceau stains in Supplementary Fig. 2. Each sample represents one pooled litter. N = 3 samples per condition. Data Presentation: All data presented as mean ± SEM. P values from two-way ANOVA with Sidak correction for (**A**).

https://doi.org/10.1038/s41593-025-01972-9

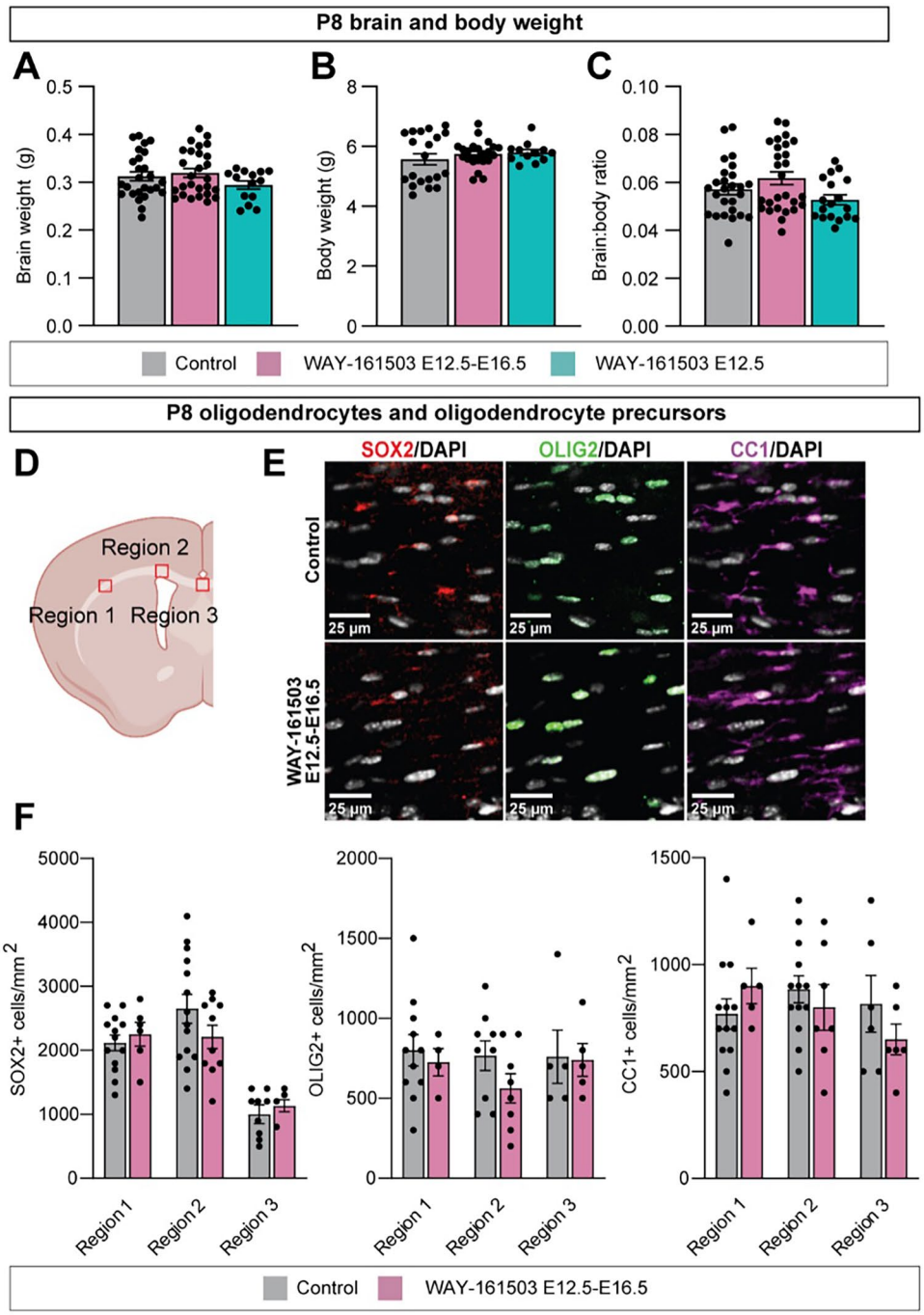

Extended Data Fig. 7 | Effects of embryonic stimulation of ChP secretion on mouse brain and oligodendrocytes. (**A**) P8 brain weight, (**B**) body weight, and (**C**) brain:body ratio in control (n = 27), repeated WAY-161503 (n = 27), and acute WAY-161503 (N = 14) mice. (**D**) Schematic, (**E**) representative confocal images, and (**F**) quantification of oligodendrocyte and oligodendrocyte precursor markers SOX2 (Region 1 control N = 13, WAY N = 6; Region 2 control N = 14, WAY N = 10; Region 3 control N = 9, WAY N = 4), OLIG2 (Region 1 control N = 11, WAY N = 4; Region 2 control N = 9, WAY N = 8; Region 3 control N = 5, WAY N = 5), and CC1 (Region 1 control N = 13, WAY N = 5; Region 2 control N = 9, WAY N = 8; Region 3 control N = 6, WAY N = 6), in the corpus callosum. Data Presentation: All data presented as mean ± SEM. P values from one-way ANOVA with Tukey correction for (**A**), (**B**), and (**C**), and from two-way ANOVA with Sidak correction for (**F**).

https://doi.org/10.1038/s41593-025-01972-9

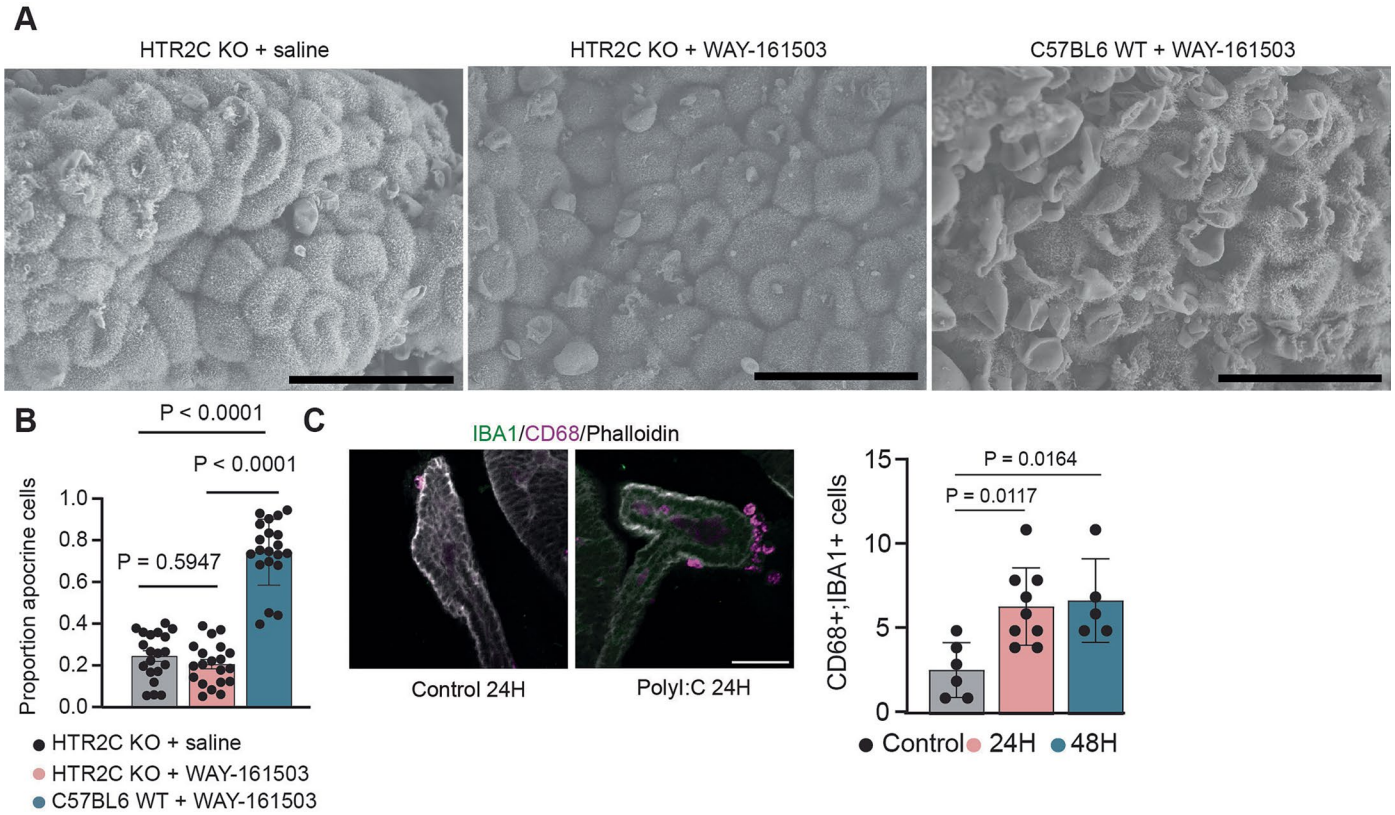

Extended Data Fig. 8 | HTR2C receptor is not necessary for baseline rates of ChP apocrine secretion. (**A**) Representative SEM of E16.5 *Htr2c* KO mouse LV ChP 30 min after maternal injection of a vehicle control (*left*), WAY-161503 (*middle*), and a C57BL6/J WT mouse after WAY-161503 (*right*). scale bars 30 µm. (**B**) Quantification of aposomes. N = 20 mice from 4 litters. (**C**) Representative confocal images and quantification of epiplexus immune cells after maternal saline (N = 6) or PolyI:C delivery (24H N = 9, 48H N = 5). Scale bar 100 µm. P values from one-way ANOVA. Data Presentation: All data presented as mean ± SEM. P values from Kruskal-Wallis test for (**B**) and from one-way ANOVA with Tukey correction for (**C**).

nature portfolio

Corresponding author(s): Maria Lehtinen

Last updated by author(s): 3/10/2025

Reporting Summary

Nature Portfolio wishes to improve the reproducibility of the work that we publish. This form provides structure for consistency and transparency in reporting. For further information on Nature Portfolio policies, see our Editorial Policies and the Editorial Policy Checklist.

Statistics

For all statistical analyses, confirm that the following items are present in the figure legend, table legend, main text, or Methods section.

n/a	Confirmed	
☐	☒	The exact sample size (*n*) for each experimental group/condition, given as a discrete number and unit of measurement
☐	☒	A statement on whether measurements were taken from distinct samples or whether the same sample was measured repeatedly
☐	☒	The statistical test(s) used AND whether they are one- or two-sided *Only common tests should be described solely by name; describe more complex techniques in the Methods section.*
☒	☐	A description of all covariates tested
☐	☒	A description of any assumptions or corrections, such as tests of normality and adjustment for multiple comparisons
☐	☒	A full description of the statistical parameters including central tendency (e.g. means) or other basic estimates (e.g. regression coefficient) AND variation (e.g. standard deviation) or associated estimates of uncertainty (e.g. confidence intervals)
☐	☒	For null hypothesis testing, the test statistic (e.g. *F*, *t*, *r*) with confidence intervals, effect sizes, degrees of freedom and *P* value noted *Give P values as exact values whenever suitable.*
☒	☐	For Bayesian analysis, information on the choice of priors and Markov chain Monte Carlo settings
☒	☐	For hierarchical and complex designs, identification of the appropriate level for tests and full reporting of outcomes
☒	☐	Estimates of effect sizes (e.g. Cohen's *d*, Pearson's *r*), indicating how they were calculated

Our web collection on statistics for biologists contains articles on many of the points above.

Software and code

Policy information about availability of computer code

Data collection	Olympus FV31S-SQ (FluoView, version 2.6) Noldus EthoVision XT videotracking software (version 9.0, Noldus Information Technologies, Leesburg, VA) Avisoft Recorder (version 2.97; Avisoft Bioacoustics)
Data analysis	Sonotrack Call Classification Software (version 1.4.7, Metris B.V., Netherlands). Observer XT software (version 9.0, Noldus) R versions 3.6.3 and 4.1.2 Biodock.AI ImageJ/FIJI Version 2.9.0/1.55i Ingenuity Pathway Analysis (QIAGEN Inc.) GraphPad Prism 9 and 10 QuPath Version 0.5.0 Ggplot2 Version 3.4.0 Dplyr Version 1.1.0 Tidyr Version 1.3.0 Zen Black 3.6 Zen Blue 3.7 Readat Version 0.7.0 Limma version 3.52.0 Biobase version 2.58.0

Countdata version 1.0.0
Ggrepel version 0.9.2
topGO version 2.48.0
org.Hs.eg.db version 3.14.0
glue version 1.6.2
tibble version 3.1.8
Rgraphviz version 2.38.0
Enrichplot Version 1.14.2
DOSE version 3.22.1
Ggvenn version 0.1.9
Ggpubr version 0.6.0

For manuscripts utilizing custom algorithms or software that are central to the research but not yet described in published literature, software must be made available to editors and reviewers. We strongly encourage code deposition in a community repository (e.g. GitHub). See the Nature Portfolio guidelines for submitting code & software for further information.

Data

Policy information about availability of data

All manuscripts must include a data availability statement. This statement should provide the following information, where applicable:

- Accession codes, unique identifiers, or web links for publicly available datasets
- A description of any restrictions on data availability
- For clinical datasets or third party data, please ensure that the statement adheres to our policy

We have made our SomaScan proteomics data publicly accessible through Zenodo at https://zenodo.org/records/10465931. scRNAseq data previously published and used in analyses can be accessed via https://www.ncbi.nlm.nih.gov/geo/query/acc.cgi?acc=GSE168704. Additional data that support the findings of this study are available from the corresponding author upon request (Maria.lehtinen@childrens.harvard.edu). Source data are provided with this paper.

Research involving human participants, their data, or biological material

Policy information about studies with human participants or human data. See also policy information about sex, gender (identity/presentation), and sexual orientation and race, ethnicity and racism.

Reporting on sex and gender	NA - this information was not collected.
Reporting on race, ethnicity, or other socially relevant groupings	NA - this information was not collected.
Population characteristics	NA - no additional characteristics are available beyond the age and ventricle data provided in the manuscript text.
Recruitment	NA - Recruitment of patients for tissue donation is prohibited. Patients are also prohibited from receiving compensation for these donations.
Ethics oversight	De-identified second-trimester choroid plexus tissue samples were collected from elective pregnancy termination specimens at the UC Davis Medical Center. The samples were acquired with patient consent and in strict observance of legal and institutional ethical regulations. Research protocols were approved by the Institutional Review Board at University of California, Davis (UC Davis IRB Protocol #2194800-1). No federal or state funding was used for these experiments.

Note that full information on the approval of the study protocol must also be provided in the manuscript.

Field-specific reporting

Please select the one below that is the best fit for your research. If you are not sure, read the appropriate sections before making your selection.

☒ Life sciences ☐ Behavioural & social sciences ☐ Ecological, evolutionary & environmental sciences

For a reference copy of the document with all sections, see nature.com/documents/nr-reporting-summary-flat.pdf

Life sciences study design

All studies must disclose on these points even when the disclosure is negative.

Sample size	To achieve robust and unbiased results, we performed our analyses across multiple samples, we prospectively randomized treatment group via random number generation, quantified results depending on genotype in a double-blinded manner and performed rigorous pre- and posthoc statistical analyses to test our hypotheses. We consulted regularly with statisticians at Harvard (BCH, BIDMC, Broad) to ensure proper calculations of power analyses and statistical methods, including accounting for multiple comparisons and covariates. We performed an equal number of experiments on males and females and carefully examined sex as a biological variable in our analyses. For each experiment, pilot studies were used to determine variance, and two-tailed power analyses determined optimal group size for alpha = 0.05 and beta = 0.80. Biological replicates (N) were defined as samples from distinct individual animals, analyzed either in the same experiment or within multiple experiments, with the exception when individual animal could not provide sufficient sample (i.e., CSF), in which case multiple animals were

pooled into one biological replicate and the details are stated in the corresponding figure legends.

Statistical analyses were performed using Prism (GraphPad) or R. Outliers were excluded using the ROUT method (Q = 1%).
Data distribution was assessed using the Shapiro-Wilk normality test, and homogeneity of variances between datasets was evaluated using F tests or Bartlett's tests. Parametric tests were used when data were normally distributed, and variances were approximately equal; otherwise, nonparametric alternatives were applied.

Specific statistical tests were selected based on the data and analysis goals: Student's two-tailed unpaired t test was used for comparisons with one independent variable and two groups, provided data followed a normal distribution and variances were equal. If variances were unequal, Welch's two-tailed unpaired t test was applied. One-way ANOVA with Tukey post hoc correction was used for analyses with one independent variable and more than two groups, provided data followed a normal distribution. Two-way ANOVA with Sidak post hoc correction was used when two independent variables were tested. Nonparametric alternatives were used for data that did not follow a normal distribution: the Mann-Whitney U test for comparisons of two groups and the Kruskal-Wallis test with Dunn's multiple comparisons correction for more than two groups. For cell density and regional quantifications, tests were selected based on the relevance of interactions between variables. In cases where exploring interactions was not relevant, multiple t tests or one-way ANOVA were used.

Data are presented as means±standard errors of the mean. Please refer to figure legends for sample size. p values < 0.05 were considered significant. Exact P values are marked in the figures where space allows.

Data exclusions

No data were excluded from analysis.

Replication

All experiments were replicated in at least two independent experiments for a total of at least 3 mice per group, and all replication was successful. All representative images are representative of the same experiment performed in at least 3 animals. For embryonic experiments, all data are the result of at least three distinct litters.

Randomization

To achieve robust and unbiased results, we performed our analyses across multiple samples, and we prospectively randomized treatment group via random number generation.

Blinding

We quantified results depending on genotype in a double-blinded manner and performed rigorous pre- and post-hoc statistical analyses to test our hypotheses. Investigators were blinded to group allocation during data collection.

Reporting for specific materials, systems and methods

We require information from authors about some types of materials, experimental systems and methods used in many studies. Here, indicate whether each material, system or method listed is relevant to your study. If you are not sure if a list item applies to your research, read the appropriate section before selecting a response.

Materials & experimental systems

n/a	Involved in the study
☐	☒ Antibodies
☒	☐ Eukaryotic cell lines
☒	☐ Palaeontology and archaeology
☐	☒ Animals and other organisms
☒	☐ Clinical data
☒	☐ Dual use research of concern
☒	☐ Plants

Methods

n/a	Involved in the study
☒	☐ ChIP-seq
☒	☐ Flow cytometry
☒	☐ MRI-based neuroimaging

Antibodies

Antibodies used

Acetylated Tubulin Mouse monoclonal IgG¬2b Clone 6-11B-1; IHC 1:200 Millipore Cat#T7451; RRID AB_609894
AQP1 Rabbit polyclonal; IHC 1:250 Millipore Cat#AB2219; RRID AB_1163380
β3-tubulin Rabbit monoclonal IgG Clone D71G9; IHC 1:250 Cell Signaling Cat#5568; RRID:AB_10694505
C-FOS Rabbit monoclonal recombinant IgG Clone Rb108B5; IHC 1:1000 Synaptic Systems Cat#226 008; RRID AB_2891278
C-FOS Mouse monoclonal IgG1 Clone E-8; IHC 1:50 Santa Cruz Cat#E-8 SC-166940; RRID AB_10609634
CC-1 Anti-APC (Ab-7) Mouse monoclonal IgG¬2b Clone CC-1; IHC 1:100 Millipore Cat#OP80; RRID AB_2057371
CC3 Cleaved Caspase-3 (Asp175) Rabbit polyclonal; IHC 1:500 Cell Signaling Cat#9661, RRID AB_2341188
CD68 Rat monoclonal Clone FA-11; IHC 1:250 Abcam Cat#ab53444; RRID AB_869007
CFL2 Cofilin 2 Rabbit monoclonal; Clone EPR25963-10; WB 1:1000 Abcam Cat#ab300128
Citrate Synthase (D7V8B) Rabbit monoclonal Clone D7V8B; IHC 1:50 Cell Signaling Cat#14309; RRID AB_2665545
CTIP2 Rat monoclonal Clone 25B6; IHC 1:250 Abcam Cat#ab18465; RRID AB_2064130
F-actin Phalloidin-iFluor 647; IHC 1:1000 Abcam Cat#ab175759
GFAP Chicken polyclonal; IHC 1:200 Abcam Cat#ab4674; RRID AB_304558
IBA1 Goat polyclonal; IHC 1:200 Abcam Cat#ab5076; RRID AB_91676
OLIG2 Human Olig2 affinity purified polyclonal; IHC 1:200 R&D Systems Cat#AF2418; RRID AB_2157554
pAKT Thr308 Rabbit; IHC 1:100 Cell Signaling Cat#9275; RRID AB_329828
pCFL2 Cofilin 2, phospho (Ser3) Rabbit Polyclonal; WB 1:1000 Abcam Cat#ab14134; RRID AB_300937
p-Histone H3 (Ser10), Mouse monoclonal Clone MC463; IHC 1:250. Millipore Cat#05-806; RRID AB_310016
SATB2 Mouse Monoclonal; Clone 2E6 IHC 1:100 Abcam Cat#ab51502; RRID AB_882455
SOD3 Mouse monoclonal IgG1 Clone 1006-2; WB 1:1000 Abcam Cat#ab80946; RRID AB_2891278

SOX2 Rabbit polyclonal; IHC 1:100 Abcam Cat#ab97959; RRID AB_2341193
Spectrin α II (C-11) Mouse monoclonal IgG1 Clone C-11; IHC 1:200 Santa Cruz Cat#sc-136074; RRID AB_671135
TBR1 Rabbit polyclonal; IHC 1:1000 Abcam Cat#ab31940; RRID AB_2200219
TTR Rabbit anti-human prealbumin; WB 1:350, IHC 1:250 Dako/Agilent Cat#A0002; RRID AB_2335696
TTR Rabbit recombinant monoclonal antibody Clone EPR21390-118; IHC 1:500, WB 1:500 Thermo Fisher Cat#MA5-47192; RRID AB_2938264
Donkey anti Goat Alexa fluor 488; IHC 1:250 Abcam Cat#AB96931; RRID AB_10680169
Goat anti Mouse Alexa fluor 594; IHC 1:250 Life Technologies Cat#A-11005; RRID AB_2534073
Goat anti Mouse Alexa fluor 647; IHC 1:250 Thermo Fisher Cat#A-21235; RRID AB_2535804
Goat anti Rabbit Alexa Fluor 488; IHC 1:250 Life Technologies Cat#A11034; RRID AB_2758380
Goat anti Rabbit Alexa Fluor 594; IHC 1:250 Abcam Cat#a11012; RRID AB_2534079
Goat anti Rat Alexa fluor 568; IHC 1:250 Life Technologies Cat#A-11077; RRID AB_2534121
Goat anti Rabbit HRP; WB 1:1000 Life Technologies Cat#31460; RRID AB_2532095
Goat anti Mouse HRP; WB 1:1000 Life Technologies Cat#31430; RRID AB_228307

Validation

Each antibody was validated for mouse use and application (immunohistochemistry, western blot) by the corresponding manufacturer. Our usage is described in full detail the methods section of the manuscript.

Animals and other research organisms

Policy information about studies involving animals; ARRIVE guidelines recommended for reporting animal research, and Sex and Gender in Research

Laboratory animals	Mouse: C57/BL6 Bred in-house or obtained from Charles River Laboratories RRID:MGI:7264769 Mouse: CD-1 Bred in-house or obtained from Charles River Laboratories RRID:MGI:5649524 Mouse: B6.129-Htr2ctm1Jke/J Gifted from Joel Elmquist at UT Southwestern and then bred in-house. RRID:IMSR_JAX:015821 Mouse: FoxJ1-CRE Zhang et al, 20074 Mouse: Ai95D(RCL-GCaMP6f)-D Jackson Laboratory RRID:IMSR_JAX:028865
Wild animals	This study did not involve wild animals.
Reporting on sex	We performed an equal number of experiments on males and females and carefully examined sex as a biological variable in our analyses.
Field-collected samples	This study did not involve field-collected samples.
Ethics oversight	The Boston Children's Hospital IACUC approved all experiments involving mice in this study on protocol 00002094 for adult experiments and 00002095 for embryonic experiments.

Note that full information on the approval of the study protocol must also be provided in the manuscript.

Plants

Seed stocks	NA
Novel plant genotypes	NA
Authentication	NA